

AD A088591

LEVEL II

(12)

RADC-TR-80-132
Final Technical Report
April 1980



HIGH POWER MILLIMETER WAVE AMPLIFIER

Varian Associates, Inc.

Sponsored by
Defense Advanced Research Projects Agency (DoD)
ARPA Order No. 3192

APPROVED FOR PUBLIC RELEASE; DISTRIBUTION UNLIMITED

The views and conclusions contained in this document are those of the authors and should not be interpreted as necessarily representing the official policies, either expressed or implied, of the Defense Advanced Research Projects Agency or the U.S. Government.

ROME AIR DEVELOPMENT CENTER
Air Force Systems Command
Griffiss Air Force Base, New York 13441

DTIC
ELECTE
SEP 3 1980
A

DDC FILE COPY

80 9 2 071

4-7

This report has been reviewed by the RADC Public Affairs Office (PA) and is releasable to the National Technical Information Service (NTIS). At NTIS it will be releasable to the general public, including foreign nations.

RADC-TR-80-132 has been reviewed and is approved for publication.

APPROVED:

Kevin O'Brien

KEVIN O'BRIEN, 1Lt, USAF
Project Engineer

If your address has changed or if you wish to be removed from the RADC mailing list, or if the addressee is no longer employed by your organization, please notify RADC (OCTP), Griffiss AFB NY 13441. This will assist us in maintaining a current mailing list.

Do not return this copy. Retain or destroy.

UNCLASSIFIED

SECURITY CLASSIFICATION OF THIS PAGE (When Data Entered)

REPORT DOCUMENTATION PAGE		READ INSTRUCTIONS BEFORE COMPLETING FORM
1. REPORT NUMBER RADC-TR-80-132	2. GOVT ACCESSION NO. AD-A088 591	3. RECIPIENT'S CATALOG NUMBER 9
4. TITLE (and Subtitle) HIGH POWER MILLIMETER WAVE AMPLIFIER		5. TYPE OF REPORT & PERIOD COVERED Final Technical Report. Oct 77 - Oct 79
6. AUTHOR(S) P. Ferguson A. Nordquist S. Hegji R. Symons H. Jory		7. PERFORMING ORG. REPORT NUMBER N/A
8. PERFORMING ORGANIZATION NAME AND ADDRESS Varian Associates, Inc., Microwave Tube 611 Hansen Way Palo Alto CA 94303		9. CONTRACT OR GRANT NUMBER(S) F30602-78-C-0011
10. CONTROLLING OFFICE NAME AND ADDRESS Defense Advanced Research Projects Agency 1400 Wilson Blvd Arlington VA 22209		11. PROGRAM ELEMENT, PROJECT, TASK AREA & WORK UNIT NUMBERS 62301E C1920004
12. MONITORING AGENCY NAME & ADDRESS (if different from Controlling Office) Rome Air Development Center (OCTP) Griffiss AFB NY 13441		13. REPORT DATE April 1980
14. DISTRIBUTION STATEMENT (of this Report) Approved for public release; distribution unlimited.		15. NUMBER OF PAGES 90
16. DISTRIBUTION STATEMENT (of the abstract entered in Block 20, if different from Report) Same		17. SECURITY CLASS. (of this report) UNCLASSIFIED
18. SUPPLEMENTARY NOTES RADC Project Engineer: Kevin O'Brien, 1Lt, USAF		15a. DECLASSIFICATION DOWNGRADING SCHEDULE N/A
19. KEY WORDS (Continue on reverse side if necessary and identify by block number) Gyrotron Traveling Wave Tube Millimeter Wave High Power Dominant Mode Circular Polarization		
20. ABSTRACT (Continue on reverse side if necessary and identify by block number) This final report describes Phase II of a program to develop a high power 94GHz amplifier based on the Gyrotron or cyclotron resonance interaction. Ultimate goals are 100 kW peak power, 10 kW average power, at least 4% bandwidth, 30% efficiency and 40 dB power gain. The experimental work in Phase II was performed at C-band (5.0GHz) to demonstrate feasibility of this approach. Following a brief review of the program as presented in the first section, the final		

DD FORM 1 JAN 73 1473 EDITION OF 1 NOV 65 IS OBSOLETE

UNCLASSIFIED

(Cont')

SECURITY CLASSIFICATION OF THIS PAGE (When Data Entered)

406552

609

UNCLASSIFIED

SECURITY CLASSIFICATION OF THIS PAGE(When Data Entered)

Item 20 (Cont'd)

testing of the 3-cavity Gyroklystron developed in Phase I is described in section 2 of this report. In section 3, a complete description including test results of the 5 GHz Gyro-TWT is given. Operating the Gyro-TWT at 60 kV beam voltage at 5 amperes beam current yielded 50 kW output power with 18 dB saturated gain (24 dB small signal gain) at 6% bandwidth and 16.6% efficiency. Small signal gain and beam mode-RF mode dispersion curves are presented in section 4. A ratio of perpendicular to parallel momentum of 1.5 yielded excellent agreement between the theoretical and experimental results. An alternate technique for producing an electron beam with a ratio of 1.5 was also investigated. This technique includes the utilization of a Pierce-type electron gun to give a solid beam (as opposed to the hollow beam produced by the conventional magnetron gun) followed by a bifilar helix of established length to impart a prescribed perpendicular velocity to the beam. This technique gives a velocity spread of 1-2% as opposed to the 8-10% spread from the magnetron gun. This should result in greatly improved output power, gain and efficiency. Future efforts should be centered around this approach.

Accession For	
NTIS Grant	<input checked="checked" type="checkbox"/>
DDC Tab	<input type="checkbox"/>
Unpublished	<input type="checkbox"/>
Justification	
F.	
Distribution/	
Availability Codes	
Dist	Available and/or Special
A	

UNCLASSIFIED

SECURITY CLASSIFICATION OF THIS PAGE(When Data Entered)

HIGH POWER MILLIMETER WAVE AMPLIFIER

P. Ferguson
S. Hegji
H. Jory
A. Nordquist
R. Symons

Contractor: Varian Associates, Inc.
Contract Number: F30602-78-C-0011
Effective Date of Contract: 28 Oct 77
Contract Expiration Date: 28 Oct 79
Short Title of Work: High Power Millimeter Wave Amplifier
Program Code Number: 7E20
Period of Work Covered: Oct 77 - Oct 79

Principal Investigator: Howard Jory
Phone: (415) 493-4000

Project Engineer: Kevin O'Brien, 1Lt, USAF
Phone: (315) 330-4381

Approved for public release; distribution unlimited.

This research was supported by the Defense Advanced Research Projects Agency of the Department of Defense and was monitored by 1Lt Kevin O'Brien (OCTP), Griffiss AFB NY 13441 under Contract F30602-78-C-0011.

TABLE OF CONTENTS

<u>Section</u>	<u>Page</u>
1. INTRODUCTION	1
2. REVIEW OF THE PHASE I AMPLIFIER AND TEST RESULTS ...	3
3. THE GYRO-TWT	22
A. Design, Fabrication and Test: VGC-8160, S/N 1	22
B. First Rebuild and Test of the Gyro-TWT: VGC-8160, S/N 1R	28
C. Second Rebuild and Test of the Gyro-TWT: VGC-8160, S/N 1R2	34
D. Second Harmonic Test - VGC-8160 S/N 1R2	39
4. SMALL SIGNAL GAIN CALCULATIONS	40
5. HIGH IMPEDANCE CIRCUIT CALCULATIONS	46
A. Introduction	46
B. Predictions	46
6. GYRO-TWT GUN AND MAGNET DESIGNS	60
A. Gun Designs	60
B. Magnetron Gun	60
C. Pierce-Type Electron Gun with Transverse Magnetic Field	63
D. Magnetic Circuit Design	67
7. REFERENCES	76
APPENDIX	

LIST OF ILLUSTRATIONS

Figure		Figure
1.	Saturated Output-Gyroklystron	7
2.	Output Power vs Drive Power - Best Results	8
3.	Gain vs Beam Voltage	9
4.	Saturated Power vs Beam Current	11
5.	Gain vs Gun Coil Current	12
6.	Peak Output Power vs Current - Main No. 1 (Collector End)	13
7.	Peak Output Power vs Current - Main No. 2	14
8.	Peak Output Power vs Current - Main No. 3	15
9.	Peak Output Power vs Current - Main No. 4 (Anode End)	16
10.	Output Power vs Drive Frequency	17
11.	Gyrotron Input (Reflex Klystron) - S/A Log Display ..	20
12.	Gyrotron Output - S/A Log Display	21
13.	Waveguide Dispersion with Oscillation Beam Lines	26
14.	Axial Field - VGC-8160 Solenoid	27
15.	Field Profile of Longer Solenoid used for VGC-8160 S/N 1R	29
16.	Gain vs Frequency for VGC-8160 S/N 1R1	31
17.	Gain vs Beam Current for VGC-8160 S/N 1R1	32
18.	Output with Beam vs Output Without Beam VGC-8160 S/N 1R	33
19.	VGC-8160 Reflected Power Input Transition	35
20.	Gyro-TWT VGC-8160 S/N 1R2	36
21.	Comparison of Calculated and Measured Gain	37
22.	Saturated Power Output	38

LIST OF ILLUSTRATIONS (CONT'D)

23.	Gyro-TWT Dispersion Relation for $\Omega_o/\omega_n = 1.05$, $\beta_1/\beta_n = 1.5$	44
24.	Calculated Gain in dB/cm vs Frequency	45
25.	Transmission Line with Periodic Loading and Increase Transverse Impedance	47
26.	Brillouin-Type Diagram for Transmission Line with Periodic Loading by Either Lumped Series Inductances or Shunt Capacitances; Case 1, Constant Ratio of B to Y_o or X to Z_o	49
27.	Normalized Transverse Impedance or Admittance Predictions for Case of Figure 26, Evaluated Midway Between Loading Elements	50
28.	Normalized Transverse Impedance or Admittance Predictions for Case of Figure 26, Evaluated in Plane of Loading Element	52
29.	Brillouin-Type Diagram for Transmission Line with Periodic Loading by Either Lumped Series Inductances or Shunt Capacitances; Case 2, ratio B/ Y_o or X/ Y_o is Proportional to Electrical Length ϕ	53
30.	Normalized Transverse Impedance or Admittance Predictions for Case of Figure 29, Evaluated Midway Between Loading Elements	54
31.	Normalized Transverse Impedance or Admittance Predictions for Case of Figure 29, Evaluated in Plane of Loading Elements	55
32.	Brillouin-Type Diagram for Corrugated Transmission Line	56
33.	Normalized Transverse Impedance or Admittance Predictions for Case of Figure 32	57
34.	Electron Trajectories for a Twenty-Three Degree Cathode Angle with a Short Front Focus Electrode	62
35.	Electron Trajectories for a Twenty-Three Degree Cathode Angle with a Medium Front Focus Electrode ...	62
36.	Electron Trajectories for a Twenty-Three Degree Cathode Angle with a Long Front Focus Electrode	62

LIST OF ILLUSTRATIONS (CONT'D)

37.	Electron Trajectories for a Five Ampere Per Square Centimeter Cathode Loading Design	64
38.	Schematic Layout of 94 GHz Gyro-TWT using a Pierce-Type Gun	66
39.	$\beta_{\perp}/\beta_{\parallel}$ vs Normalized Helix Length for Three Electron Rays for $B/B_0 = 0.5\%$	68
40.	Computed Electron Trajectories for the Pierce-Type Diode Gun - Zero Magnetic Field	70
41.	Superconducting Solenoid Field for 94 GHz Tube	72
42.	95 GHz Gyro-TWT Solenoid, Nutcracker Run 4.5	73
43.	Computed Electron Trajectories for the Pierce-Type Diode Gun for a Magnetic Field with Iron Polepiece ID = 1.67", Located 0.18" from Cathode Center	74
44.	Computed Electron Trajectories for the Pierce-Type Diode Gun for a Magnetic Field with Iron Polepiece ID = 2.09", Located 0.27" from Cathode Center	75

1. INTRODUCTION

This report describes Phase II of a program to develop a high-power 94 GHz amplifier. The ultimate goals were:

Center Frequency	94 GHz
Bandwidth	>4%
Peak Power	100 kW
Average Power	10 kW
Beam Efficiency	30%
Power Gain	30 dB

At the outset of Phase II, it was decided that experiments should be performed at the fundamental and second harmonic interactions before proceeding to higher harmonics because of the sensitivity of efficiency to cyclotron number and because the higher harmonic interactions are expected to be more difficult to stabilize.

To minimize development time and cost, it was decided to design gyro-TWT experiments using the gyroklystron hardware from Phase I wherever possible. In particular, the existing solenoid and gun designs were used.

The present program was preceded by a Phase I study effort¹ which explored the feasibility of gyroklystron amplifiers with cyclotron harmonic operation. As part of the study effort, a three-cavity gyroklystron amplifier operating on the second harmonic of the cyclotron frequency at X-band was built and partially tested. At the beginning of Phase II the testing was completed. A review of the gyroklystron, measurements of saturated output power and spectrum, and noise figure measurements are presented in Section 2.

The design approach, fabrication techniques and test results of the 5 GHz gyro-TWT and the rebuilds are presented in Section III. Test results for second harmonic operation are also included.

In Section IV the small signal gain calculations are discussed. Attention is given to rewriting the dispersion equation for the linearly polarized TE_{11}^0 mode in a form similar to that found in TWT theory. The computed ω - β diagram and gain curve using the experimental parameters from Section 3 are also presented.

The aforementioned gyroklystron and gyro-TWT employed geometrically simple cylindrical cavities or cylindrical waveguides as interaction circuits. In order to increase the circuit-electron beam interaction, several high impedance circuits were investigated. The results are presented in Section 5.

In Section 6, the design procedure for the magnetron electron gun is discussed. The design procedure is based on techniques developed for the ongoing gyrotron programs at Varian. Finally, a detailed account is given of an alternative method of producing an electron beam with a prescribed ratio of perpendicular to parallel momentum. This method utilizes a Pierce-type electron gun to produce a solid beam (as opposed to the annular beam from a magnetron gun) followed by a bifilar helix capable of imparting a prescribed perpendicular momentum upon the beam. This technique allows for greatly reduced velocity spread, thus offering the possibility of increasing output power, gain, and efficiency.

The final test results achieved are outlined in the table below:

Performance of the Gyro-TWT, VGC-8160, S/N 1R2
Gyro-TWT (5.2 GHz)

Beam Voltage	60 kV
Beam Current	5 A
Power Output	50 kW
Small Signal Gain	24 dB
Saturated Gain	18 dB
Bandwidth (Saturated)	6% (3 dB points)
Electronic Efficiency	16.6%

2. REVIEW OF THE PHASE I AMPLIFIER AND TEST RESULTS

The amplifier which was constructed in Phase I is a three-cavity gyrokystron, for operation at 10.35 GHz. It was designed to operate at the second harmonic of the cyclotron resonance condition. The resonance condition is given by the equation

$$\omega = \frac{neB}{\gamma m_0} \quad (1)$$

where ω is the operating frequency, B is the axial dc magnetic field, e/m_0 is the charge-to-mass ratio of the electron, γ is the relativistic mass factor, and n is the harmonic number. Operation at the second harmonic of the resonance allows the magnetic field to be smaller by a factor of two. The fundamental cyclotron resonance at 94 GHz requires a magnetic field of about 33 kg and second harmonic operation requires 16.5 kg. Hence the magnitude of field required is high enough to make operation at second or third harmonic worth considering.

The operating parameters for the 10.35 GHz amplifier are given in Table I. Additional information on the design is included in the final report for Phase I ⁽¹⁾.

Initial operation resulted in the observation of a microwave gain of 9 to 10 dB under small signal conditions where the power output was about 100 W peak. This operation was achieved at reduced beam voltage of 40 kV. Amplifier operation at higher beam voltage had been prevented by interfering oscillations involving the TE_{111} resonance in the input cavity interacting with the fundamental cyclotron resonance condition. The oscillation occurred at a frequency near 5.4 GHz and was somewhat tunable depending on main magnetic field values. Table 2 shows a summary of preliminary test values compared to design values.

TABLE 1
10.35 GHz AMPLIFIER DESIGN VALUES

1.	Power output - peak	100	kw
	average	5	kW
2.	Gain	30	dB
3.	Bandwidth	0.1	%
4.	Magnetic field	1.96	kg
5.	RF circuits (TE ₀₁₁ cavities)		
	Input cavity length	1.5	λ *
	First drift length	1.2	λ
	Center cavity length	1.5	λ
	Second drift length	1.2	λ
	Output cavity length	3	λ
	Cavity loaded Q (each cavity)	1000	
	Drift tube radius (0.51)	0.58	in
6.	Beam		
	Voltage	60	kV
	Current	5	A
	Outer beam radius	0.53	in
	Inner beam radius	0.19	in
	Axial velocity	0.2	c **
	Transverse velocity	0.4	c
	Electron orbit radius	0.15	in

* λ = Free-space wavelength at the operating frequency.

** c = velocity of light

TABLE 2
SUMMARY OF PRELIMINARY TEST RESULTS

<u>Parameter</u>	<u>Design Value</u>	<u>Preliminary Test Value</u>
Beam Voltage	60 kV	40 kV
Gun anode voltage	31 kV (52%)	24 kV (60%)
Beam current	5 A	4.5 A
Main magnet field	1960 g	1960 g \pm 5%
Gun magnet	485 g	450 g \pm 10%
Microwave gain	23 - 26 dB	9 - 10 dB
Peak body current	0	80 ma
Peak gun anode current	0	<4 ma

At the start of Phase II, a linear-beam klystron capable of about 8 kw peak output power was installed as a driver for the gyroklystron, allowing the gyroklystron to be driven to saturation. Figure 1 shows a typical saturated power curve. The 40 kV, 4.0 A beam parameters were the nominal values used in the majority of the measurements performed. Higher values of beam voltage and current yielded marginal operating points and did not allow exploration of the parameter space. However, the highest values of saturated power, small signal gain, and efficiency were obtained at 50 kV and 5.0 A. The data for this result are summarized in Table 3, and the saturated power curve appears in Figure 2.

TABLE 3
BEST PERFORMANCE

<u>Parameters</u>	<u>Test Value</u>
Beam voltage	50 kV
Beam current	5.0 A
Saturated power	20.56 kw
Small signal gain	5.8 dB
Gain compression	1.4 dB
Saturated efficiency	8.2%

Eight independent variables affect the performance of the gyroklystron in test: beam voltage and current, anode voltage, the four sections of the main magnet, and the gun coil current. The first of these, beam voltage, has a limited range (if all others are held fixed) due to the onset of undesired oscillations mentioned in Section II. Figure 3 shows the result of varying the beam voltage from 35 kV to 45 kV. It should be noted that anode voltage is changing also since the ratio is fixed. It was impractical to attempt to keep anode voltage fixed, but all magnetic fields were fixed.

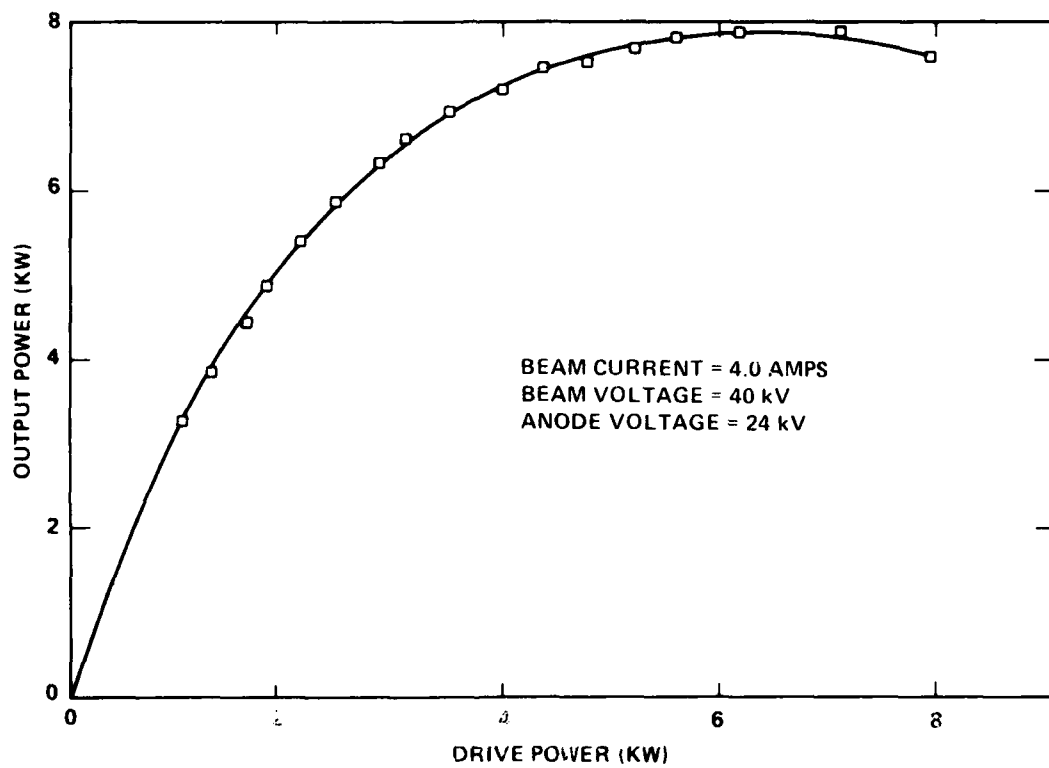


Figure 1. Saturated Output-Gyroklystron

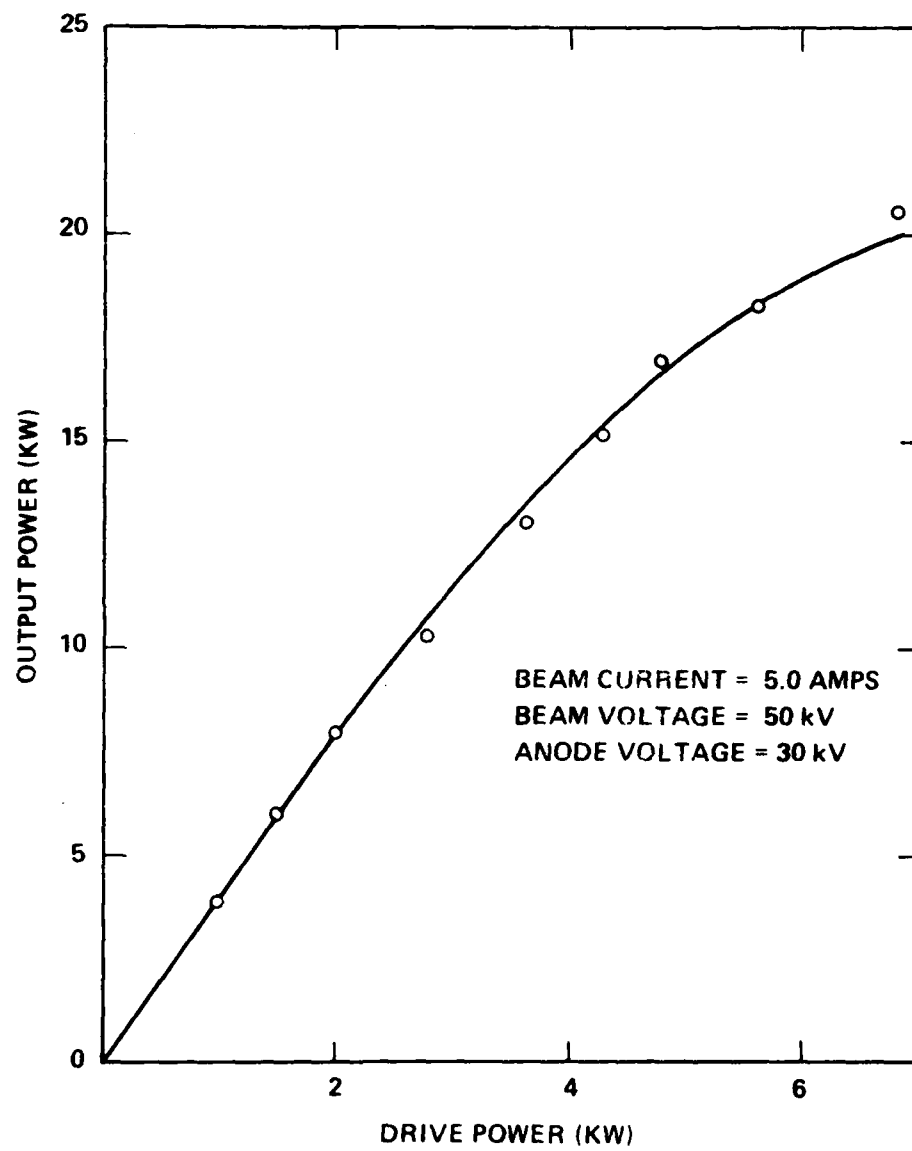


Figure 2. Output Power vs Drive Power – Best Results

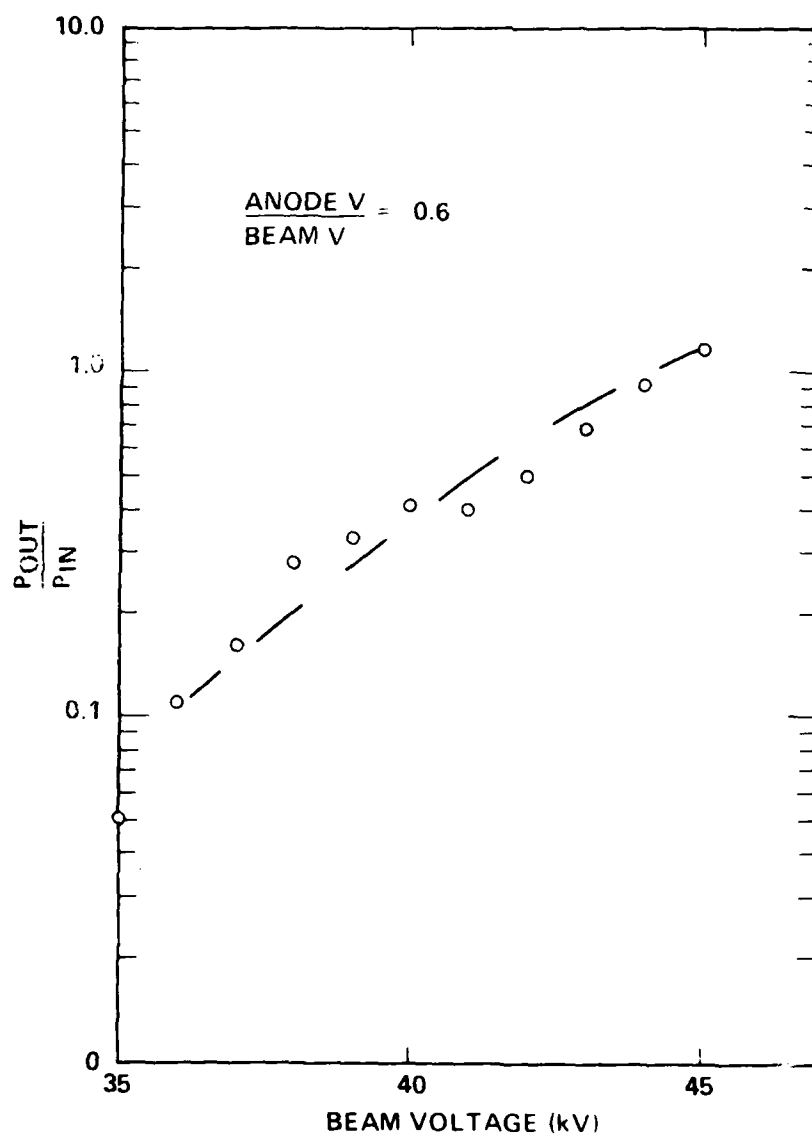


Figure 3. Gain vs Beam Voltage

The cathode is operated in a temperature-limited mode; hence, the beam current is easily varied by adjusting the heater power. Figure 4 depicts the increase in saturated output power as the beam current is increased. The regions above 5.0 A and below 3.2 A were disturbed by unstable behavior in the gun-anode region.

The magnetic field from the gun coil is the major contributor to flux threading the cathode. The flux determines, along with anode voltage, the amount of transverse energy on the beam. The gain of the gyrokystron should increase as the coil current is reduced; Figure 5 shows this effect. The total dynamic range produced is 11 dB. Lower values of gun coil current were prevented by oscillations.

Figures 6 through 9 show the variation in small-signal output power as the currents in each of the main sections are varied. The three sections closest to the collector exhibited definite maximum points of 3-6 dB. The coil closest to the anode caused a gradual increase in output as the current was raised to the supply's limit.

An investigation of bandwidth, obtained by varying the drive frequency, yielded the curve of Figure 10. The half-power bandwidth is 13 MHz.

Table 4 shows the baseline values used in the experiments which yielded Figures 4 through 10.

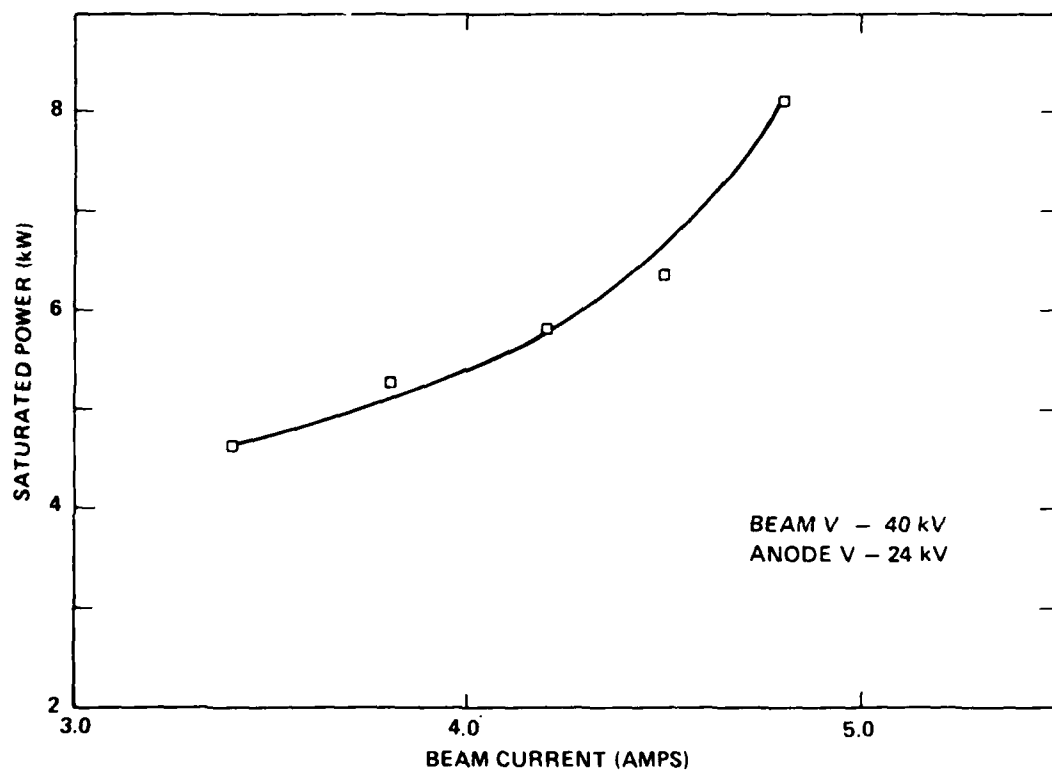


Figure 4. Saturated Power vs Beam Current

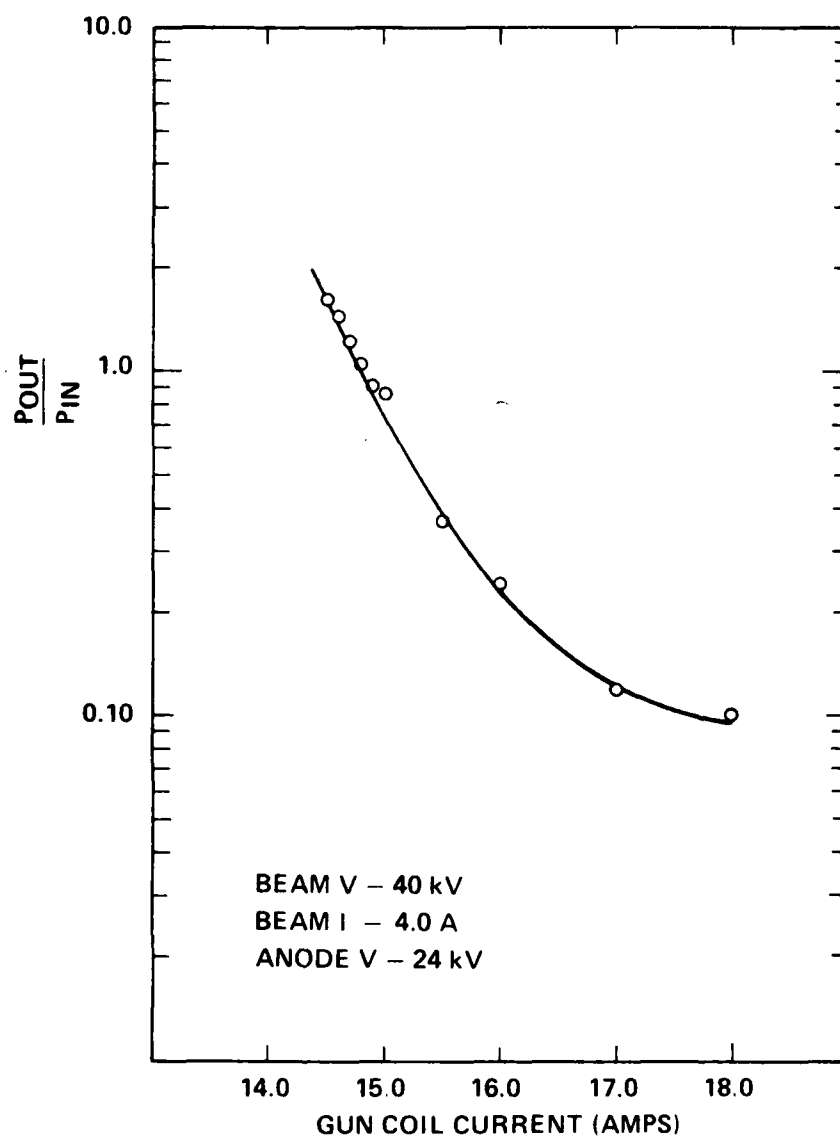


Figure 5. Gain vs Gun Coil Current

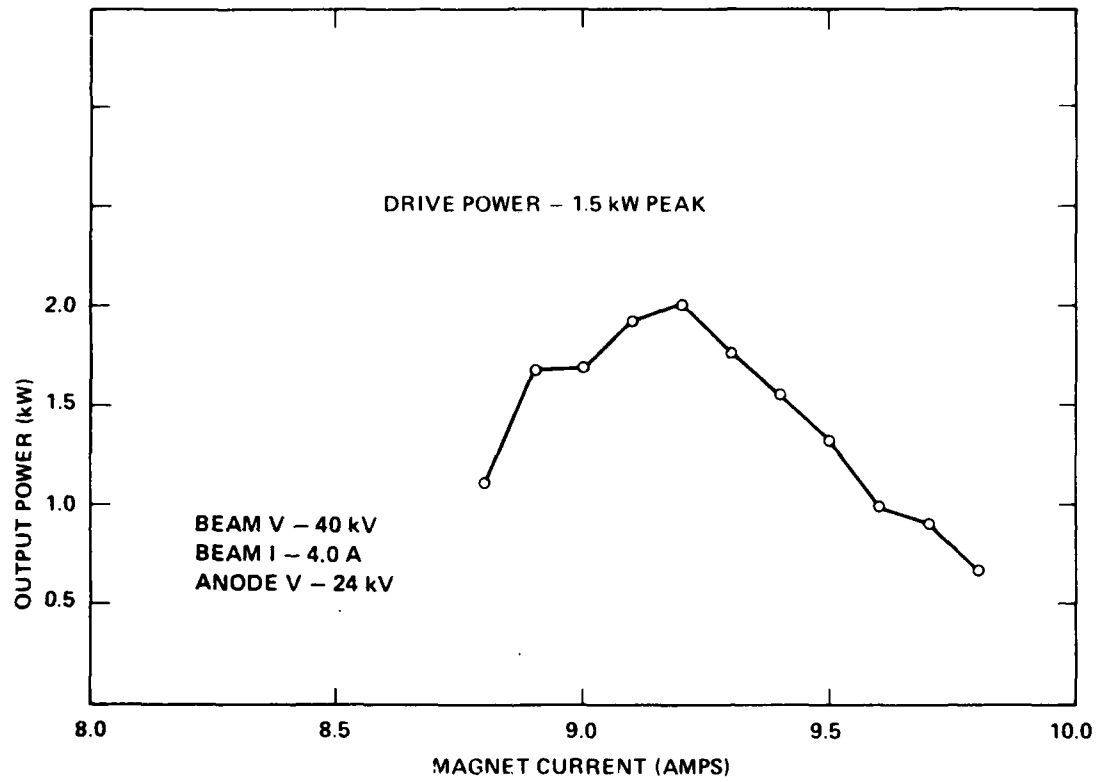


Figure 6. Peak Output Power vs Current - Main No. 1 (Collector End)

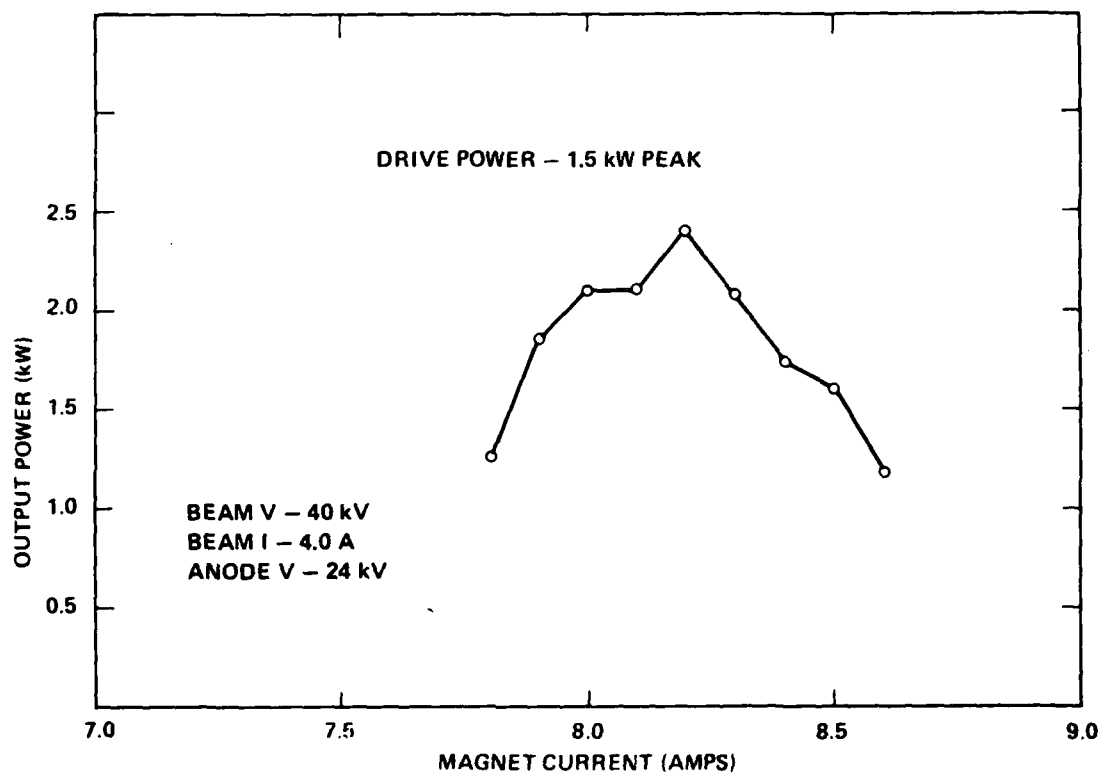


Figure 7. Peak Output Power vs Current - Main No. 2

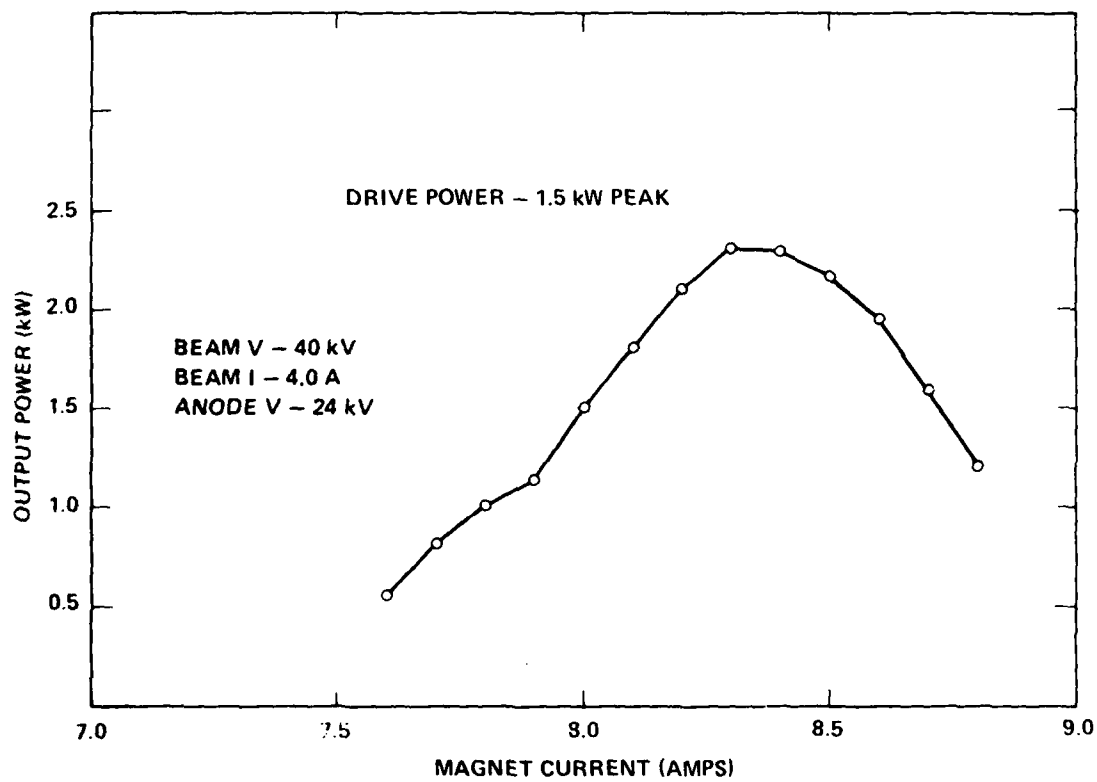


Figure 8. Peak Output Power vs Current - Main No. 3

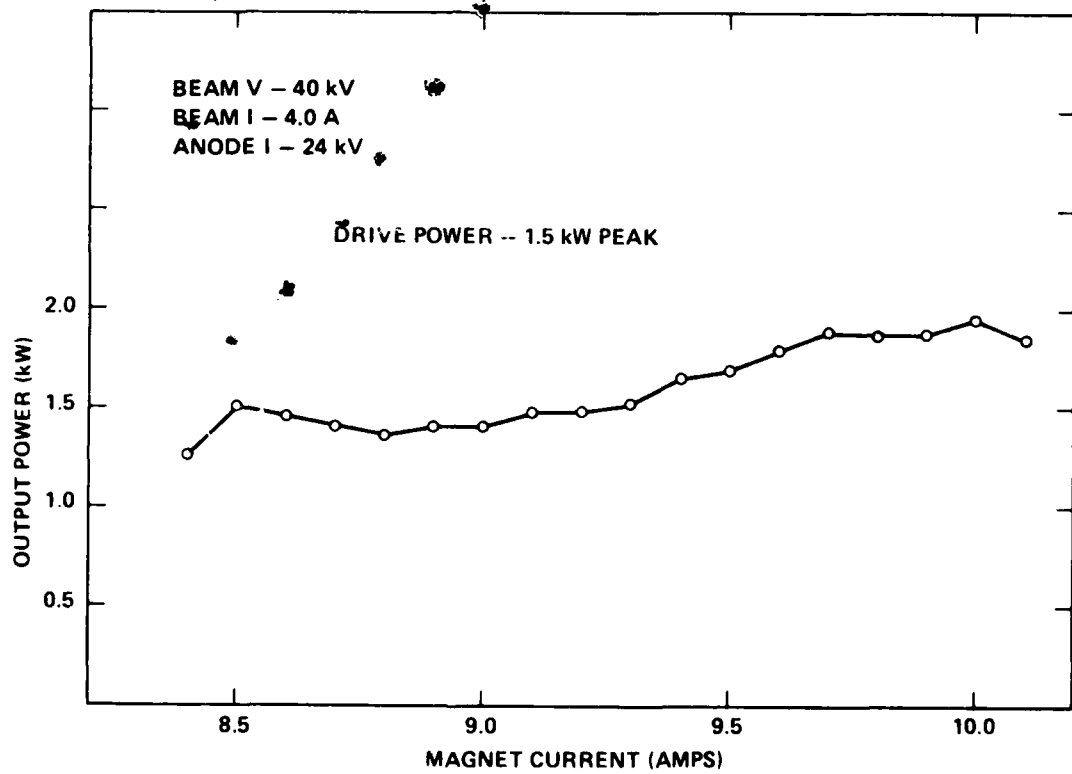


Figure 9. Peak Output Power vs Current — Main No. 4 (Anode End)

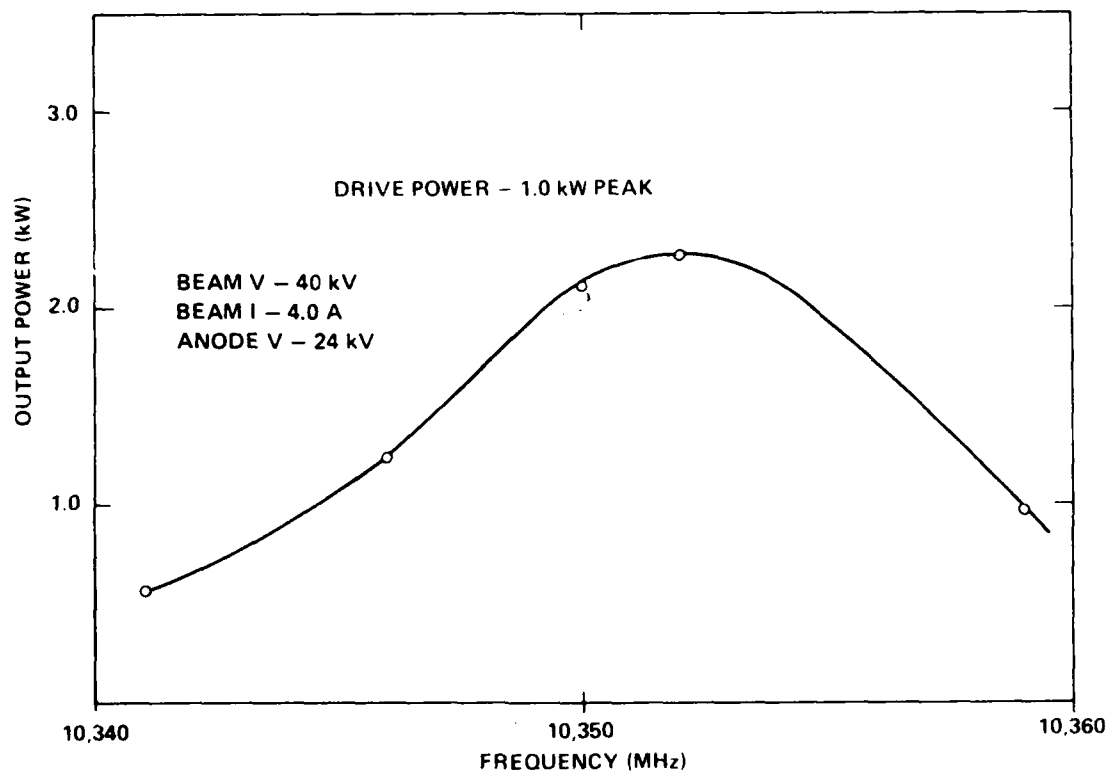


Figure 10. Output Power vs Drive Frequency

TABLE 4
NOMINAL OPERATING PARAMETERS

Beam Voltage	40.0	kV
Beam Current	4.0	A
Anode Voltage	24.0	kV
Magnet Coil Current		A
Main 1	9.3	
2	8.2	
3	8.6	
4	10.0	
Gun	14.5	

Two measurements were made pertaining to the signal quality of the gyroklystron output. The first of these was a determination of a noise figure. The gyroklystron input port was terminated in a matched load. The resulting output was mixed down and sent to an IF amplifier, and then video displayed. The output of a gas discharge tube, with a known noise figure, was gated with a PIN diode modulator and then processed through the mixer and IF amplifier. The two pulses were compared on the display. Table 5 shows the noise figures obtained at different gyrotron operating points.

TABLE 5
NOISE FIGURE*

<u>Operating Point (Small-Signal Gain)</u>	<u>Noise Figure</u>
1 dB	53 dB
6 dB	59 dB

* Noise figures are referenced to thermal noise (Johnson noise), about -204 dBw.

Spectrum analyzer displays of the gyroklystron output were recorded. A reflex klystron oscillator replaced the klystron amplifier as a drive source for the gyrotron. The output of the oscillator was gated with a PIN diode modulator. The combination provided a spectral input to the gyroklystron as shown in Figure 11. Figure 12 shows the resulting output spectrum.

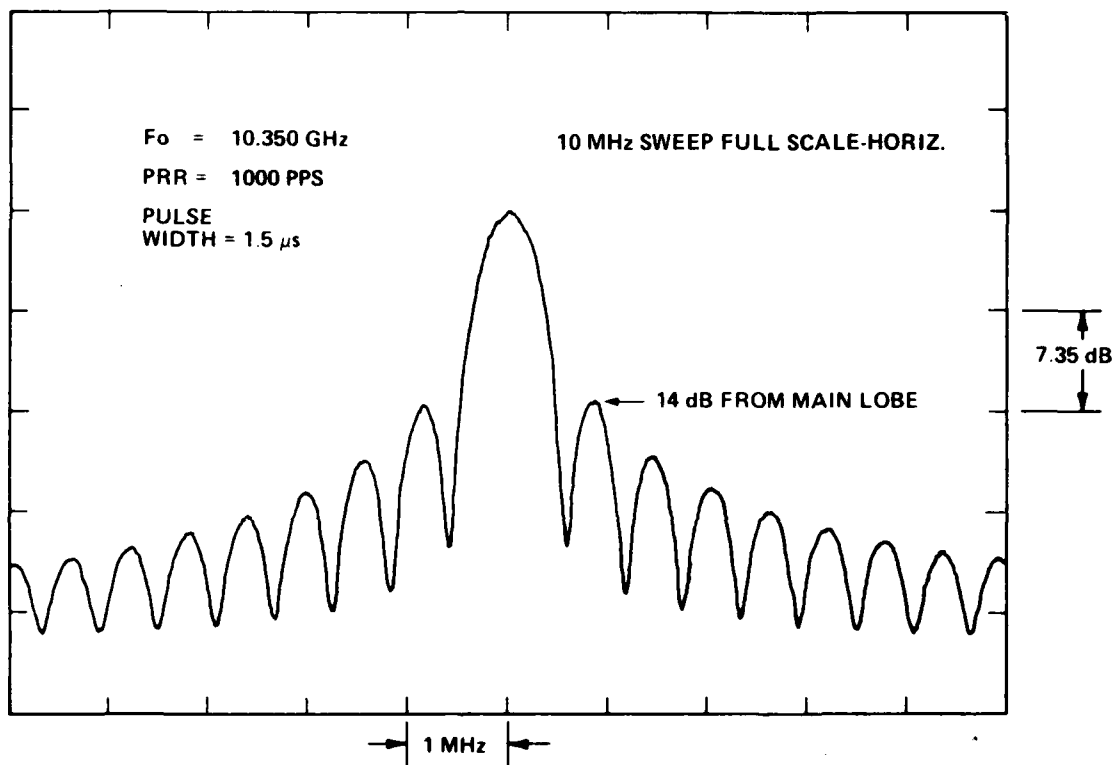


Figure 11. Gyrotron Input (Reflex Klystron) – S/A Log Display

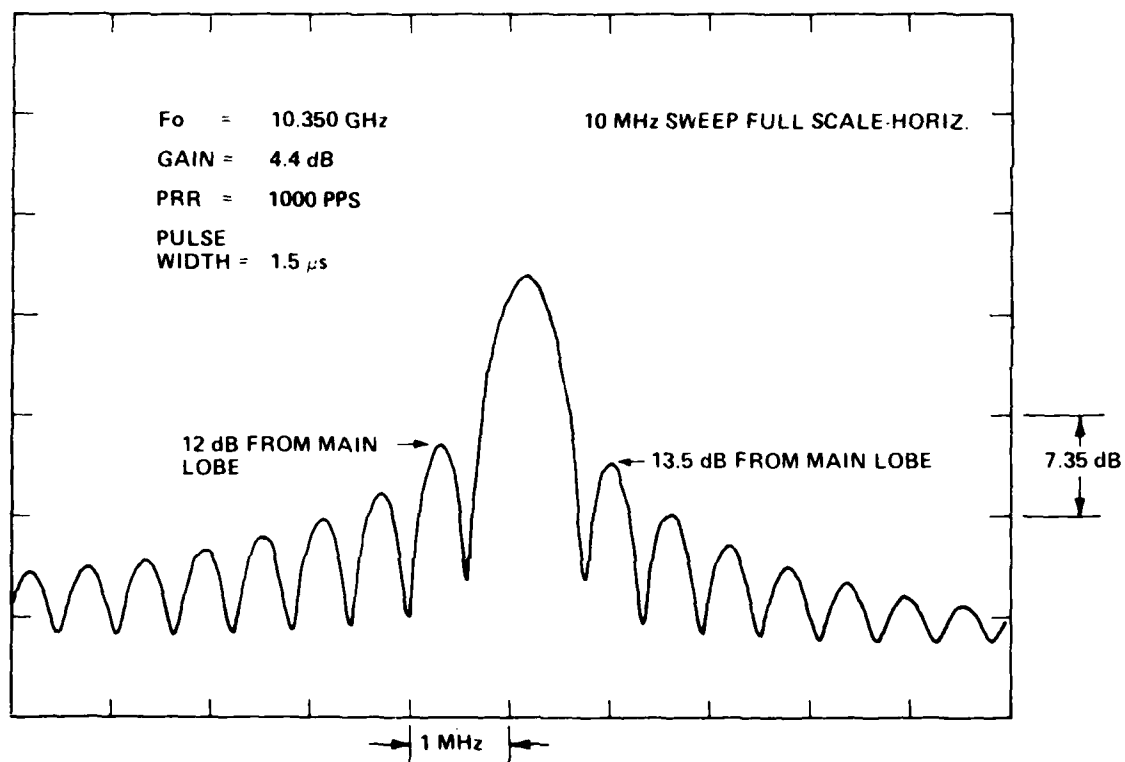


Figure 12. Gyrotron Output – S/A Log Display

3. THE GYRO-TWT

The design, fabrication and test of the gyro-TWT will be discussed in this section in chronological order.

The gyro-TWT was built and tested, then rebuilt and tested two times, each rebuild resulting in a device with higher efficiency, higher power and increased gain.

The gyro-TWT version of the family of cyclotron resonance masers differs from the klystron or monotron by virtue of its non-resonant rf circuit. The beam is well-coupled to the EM fields over a reasonable bandwidth (5-10%). Unlike a conventional (linear beam) TWT, the gyro-TWT utilizes a fast-wave interaction between circuit and beam. This allows the use of simple, non-periodic rf circuits.

A. DESIGN, FABRICATION AND TEST: VGC-8160, S/N 1

The gyro-TWT was designed to employ the TE_{11} mode in a circular guide and to operate at the fundamental cyclotron resonance, about 5.2 GHz. (10.35 GHz fundamental operation is beyond the capability of the existing solenoid.) The input coupling system had to fit within the magnet bore, which was difficult at 5.2 GHz with conventional rectangular waveguide components. An attempt was made to couple to the rf circuit using a coaxial transmission line terminated in a probe or loop. The close proximity of the beam to the wall of the interaction circuit required the use of small loops or probes which had high radiation resistances, and required excessive impedance transformation to achieve an acceptable match. A hybrid solution was found involving coupling to the circuit with a rectangular waveguide port and then using a vacuum tight coax-to-waveguide transition. The matching for the rectangular guide to the interaction circuit required a capacitance at the junction. Since two orthogonal TE_{11} modes can exist, two inputs were required separated 90° azimuthally.

When the rf circuit assemblies were completed, testing of the entire circuit revealed an input match significantly worse than the cold test

measurements predicted. Attempts were made to analyze the mismatch using Smith Chart impedance measurements across the 10% band. The results showed that the best place for a broadband improvement of the match occurred at a plane located inside the coaxial elbow-vacuum window assembly. The addition of reactive elements to the coaxial elbow assembly yielded a match better than 2:1 over a 6% band.

For the gyro-TWT experiment, using the TE_{11} mode, a change in the output window design was required. The previous window design had an axial break in the guide wall suitable for the TE_{01} mode and was matched for operation at 10.35 GHz. For use with TE_{11} mode, the axial wall gap had to be removed, and the window thickness increased to obtain a C-band match. Transmission measurements on the window revealed several trapped window modes above the band, with the lowest at the upper band edge. These were found not to be troublesome.

Table 6 shows the design values for the gyro-TWT. The rf circuit length was determined primarily by the size of the available magnet. The uncertainties in the values for output power and gain reflect the unknown character of the launching losses and the lack of good gain calculations. The rf circuit was capable of propagating two orthogonal TE_{11} modes which were sure to be coupled somewhat by the rotating beam, making the launching losses difficult to predict. At the time the tube was built, the NRL computer codes for TWT gain had not yet been transferred to Varian.

TABLE 6
5.2 GHz Gyro-TWT Design Values

1.	Power Output - peak	~100	kW
	- average	~5	kW
2.	Gain	~20-30	dB
3.	Bandwidth	5.0	%
4.	Magnetic field	1.96	kG
5.	RF Circuit (circular waveguide)		
	Guide length	5.1	λ *
	Guide radius	0.72	in
6.	Beam		
	Voltage	60	kV
	Current	5	A
	Outer beam radius	0.53	in
	Inner beam radius	0.19	in
	Axial velocity	0.2	c **
	Transverse velocity	0.4	c
	Electron orbit radius	0.15	in

* λ = Free-space wavelength at the operating frequency.

** c = velocity of light (in vacuum).

The gyro-TWT was tested into a circular waveguide load at a low rf duty (1-2%). A 10 W TWT linear beam amplifier was used to drive one of the two orthogonal inputs while the other was terminated in a matched load. An iris coupled, side wall output coupler in circular guide was used to sample the output in the two orthogonal modes. This output was measured with thermistor mounts and power bridges.

To start, two different oscillations were observed with frequencies near 4.8 and 8.0 GHz respectively. The first oscillation was smoothly tunable between 4.8 and 5.2 GHz and generated a significant amount of power (1-2 kw peak) at the input ports, which suggests it may be either a backward wave oscillation in the TE_{11} mode, or it may be due to match difficulties near the waveguide cutoff. Figure 13 shows the beam line for this oscillation plotted against the TE_{11} and TE_{01} waveguide dispersion hyperbolas for the circuit.

The other observed oscillation consisted of discrete frequencies between 8.05 and 8.55 GHz. The behavior of the oscillation was similar to that of a multi-wavelength, multi-mode cavity which oscillated at separated frequencies depending on the magnetic field value. The beam line for this mode is also plotted in Figure 13, along with its second harmonic beam line, identifying the oscillation as a TE_{21} mode oscillation at the second harmonic of the cyclotron resonance.

The axial magnetic field was adjusted to lie between the values used to obtain the two oscillations. This yielded indications of forward wave gain. After some optimization of magnetic field, and after increasing the output coupling, small signal gain measurements were taken which indicated gains of 0-3 dB across the band (4.9-5.4 GHz).

At this time, concern over the uniformity of the axial magnetic field motivated removing the tube from the socket and measuring the dc field. With all main magnet sections excited with equal currents, the axial field varied only 1.5% over a 9" length (total rf circuit length is 11"). Figure 14 shows a plot of this field. A measurement of the off axis field at the average beam diameter yielded similarly good results. Because no magnetic

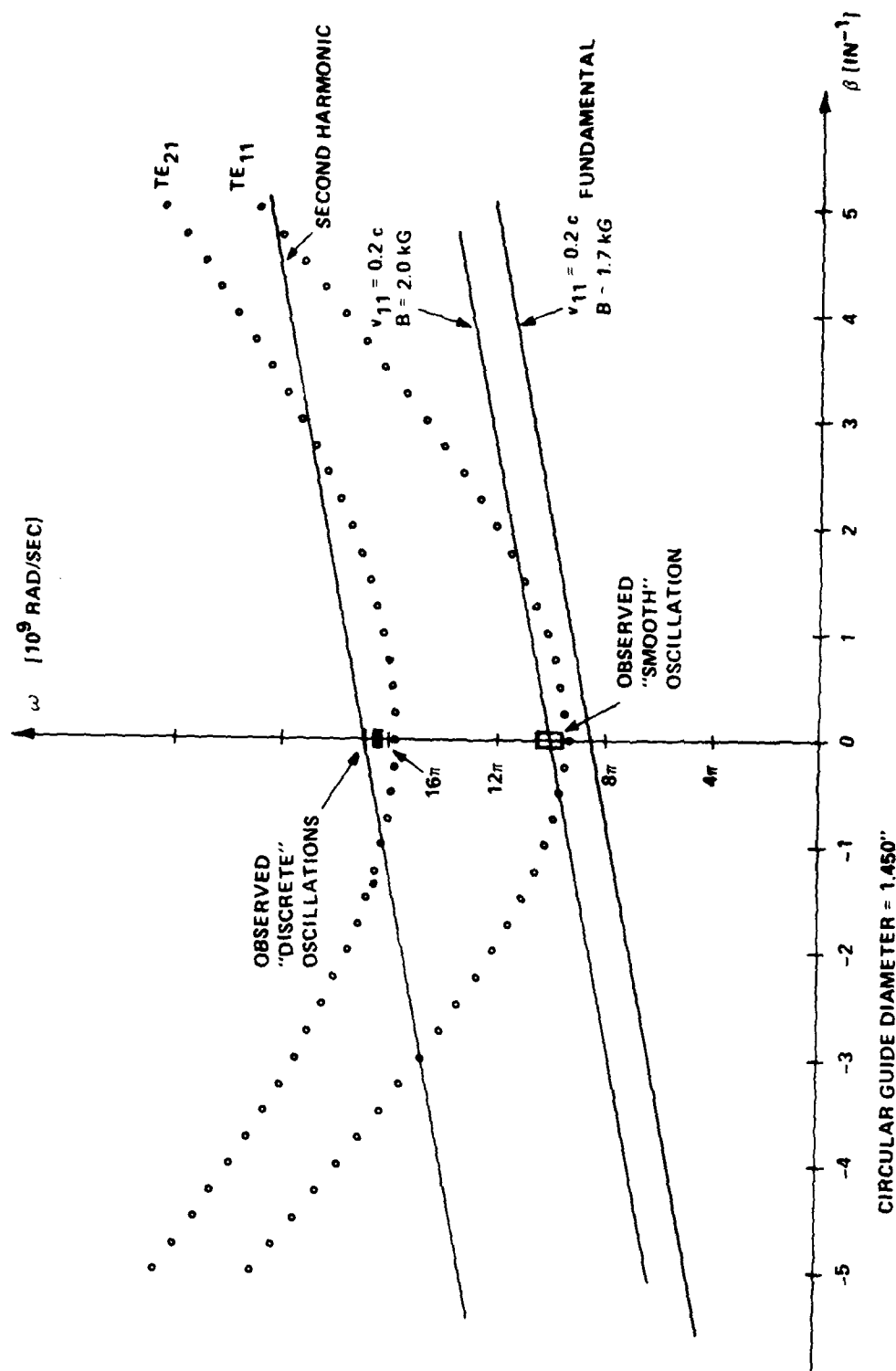


Figure 13. Waveguide Dispersion with Oscillation Beam Lines

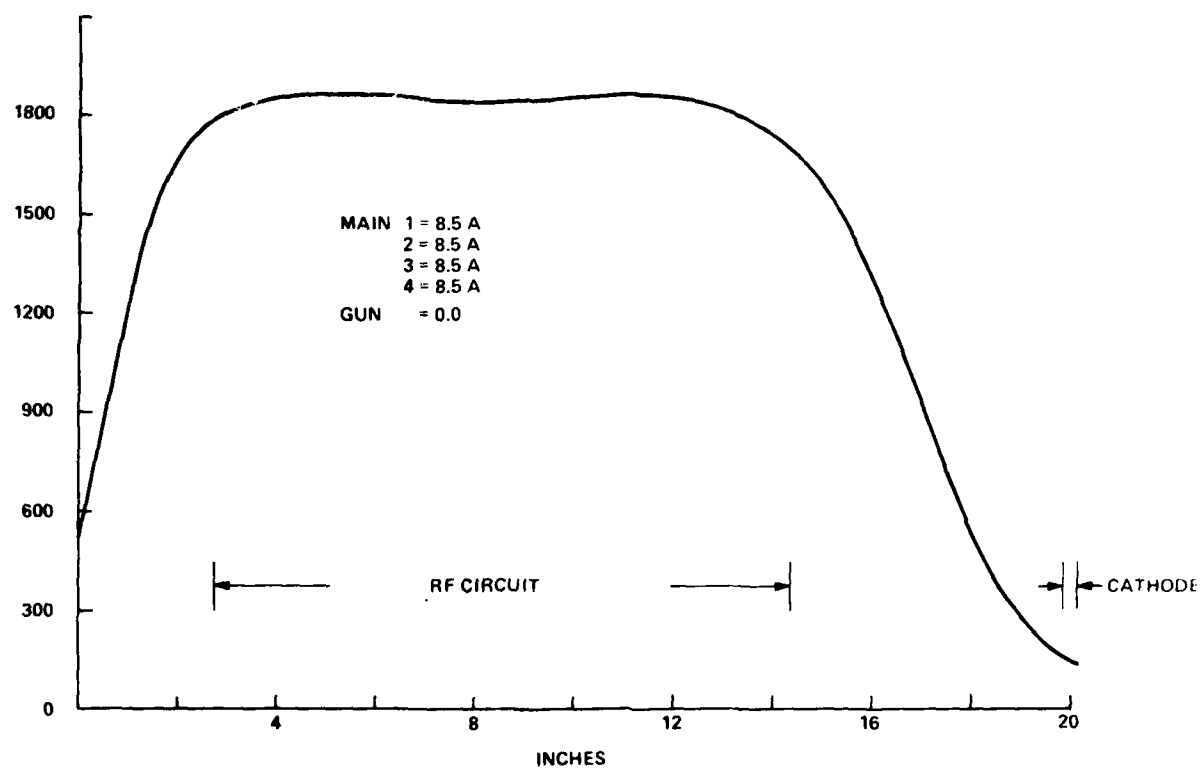


Figure 14. Axial Field -- VGC-8160 Solenoid

problems were found and because calculations indicated that the gain would not exceed the estimated launching loss by any large amount, tests were halted and work was begun on a rebuild.

B. FIRST REBUILD AND TEST OF THE GYRO-TWT: VGC-8160, S/N 1R

From the test results described in the previous section, it was concluded that the tube had only enough gain to overcome the estimated launching losses. Accordingly, a center section was designed which could be added to the tube and effectively double its interaction region. This assembly was built and incorporated into the device.

A focusing solenoid of increased length was found which accepted the new tube length; and furthermore, was capable of generating higher magnetic fields. This added feature allowed us to test the validity of the interaction theory where it concerns changes in magnetic field.

Initial tests indicated poor beam transmission. The tube was removed from the socket and the axial magnetic field profile of the new, longer solenoid was investigated. The measurements indicated insufficient field at the cathode position, so an additional coil was added to the assembly. Figure 15 shows the actual field profile achieved along with the profile used in the gun design simulations.

After verifying good beam transmission in the adjusted magnetic circuit, the tube was brought up to full operating parameters. The first rf outputs observed were oscillations occurring in the same two frequency ranges which had been observed in the original build. Specifically, the oscillations were confined to the 4.9 and 8.1 GHz regions, and were calorimetrically measured to have peak output powers of 45 kW and 14 kW respectively at a beam power of 300 kW.

When the beam's transverse energy was slightly reduced by increasing the cathode magnetic field, the onset of oscillation was discouraged and amplification was observed. Small-signal measurements yielded a maximum of 17 dB gain at 4.9 GHz, with a beam voltage of 45 kV, and a beam current of

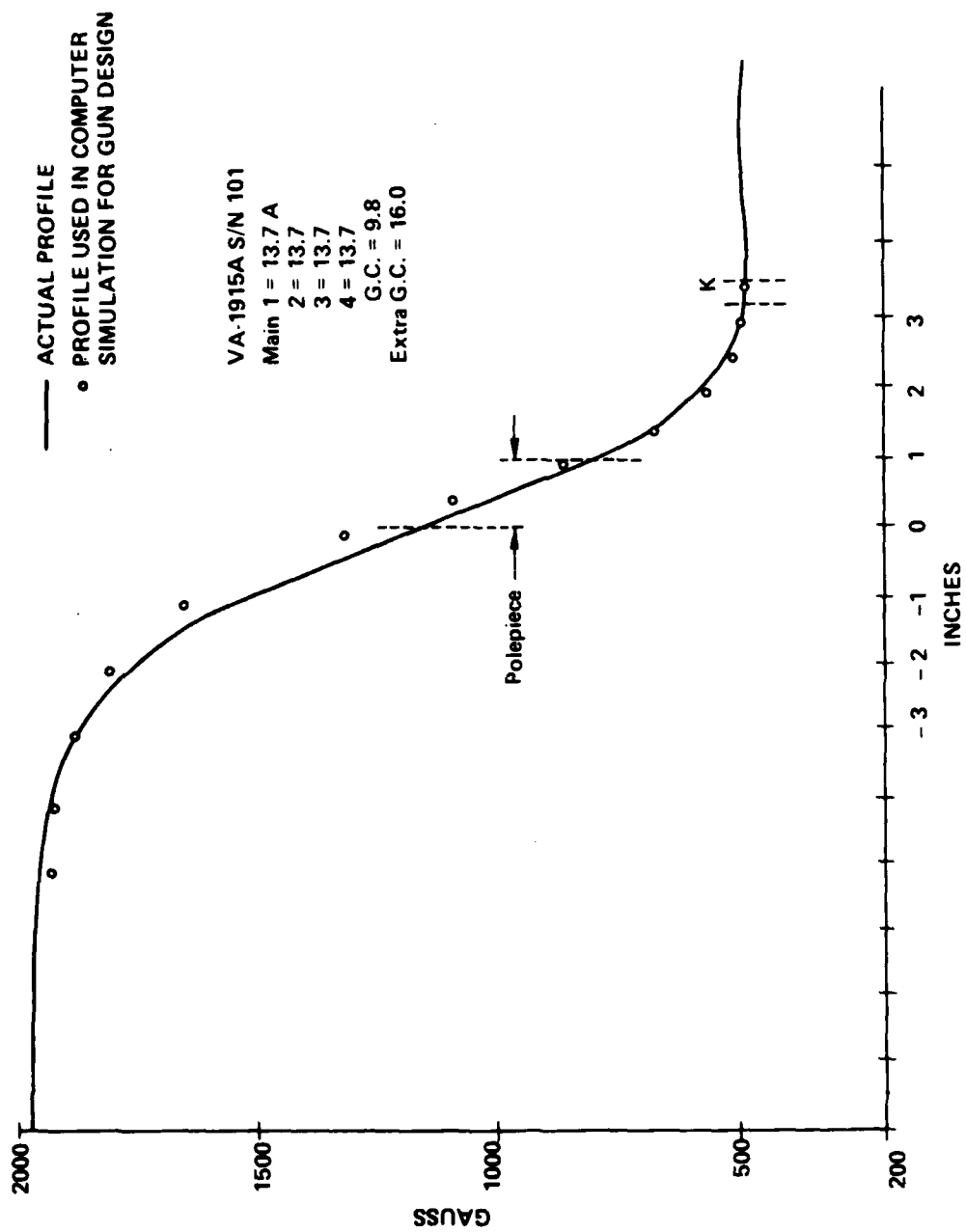


Figure 15. Field Profile of Longer Solenoid used for VGC-8160 S/N 1R

2.5 A. The low values of voltage and current tended to yield higher possible gain values. The lower total beam power allowed setting the gun magnets for higher transverse energy without the occurrence of oscillations.

Figure 16 shows the variation in small-signal gain at various frequency points over the band of detectable amplification. It was felt that the large variations in gain are associated with the poor tube match (input and output) between 4.9 and 5.1 GHz. At the higher frequencies, 5.1 to 5.3 GHz, the match was better, the interaction was weaker, and the magnetic field may not have been optimized, in order to avoid oscillation.

The dependence of gain on beam current was investigated and is shown in Figure 17. This measurement was also made at more stable values of beam transverse energy.

A high power TWT driver was installed at the gyrotron modulator. This tube (VTC-5262A), designed to deliver 5 kW between 5.4 and 5.9 GHz, proved capable of 2.5 kW at 4.9 GHz. With the driver operated at 4.9 GHz, the gyrotron's maximum gain point, a small signal gain of 17.8 dB was measured at 47 watts of drive power. As drive increased, the output saturated at 11.5 - 13.0 kW, with an electronic efficiency of 5-6%. The corresponding gain compression was 3.0 dB (see Figure 18). These data were taken at magnetic fields differentially lower than those resulting in oscillation, indicating that the gain and perhaps the saturated output could be improved if the oscillation was stabilized.

A measurement was made of the tunability of the 4.8 GHz oscillation as the main magnetic field was varied. The oscillation frequency smoothly increased from 4.8 to 5.0 GHz as the main magnet coil currents were raised from 12.0 to 15.0 A.

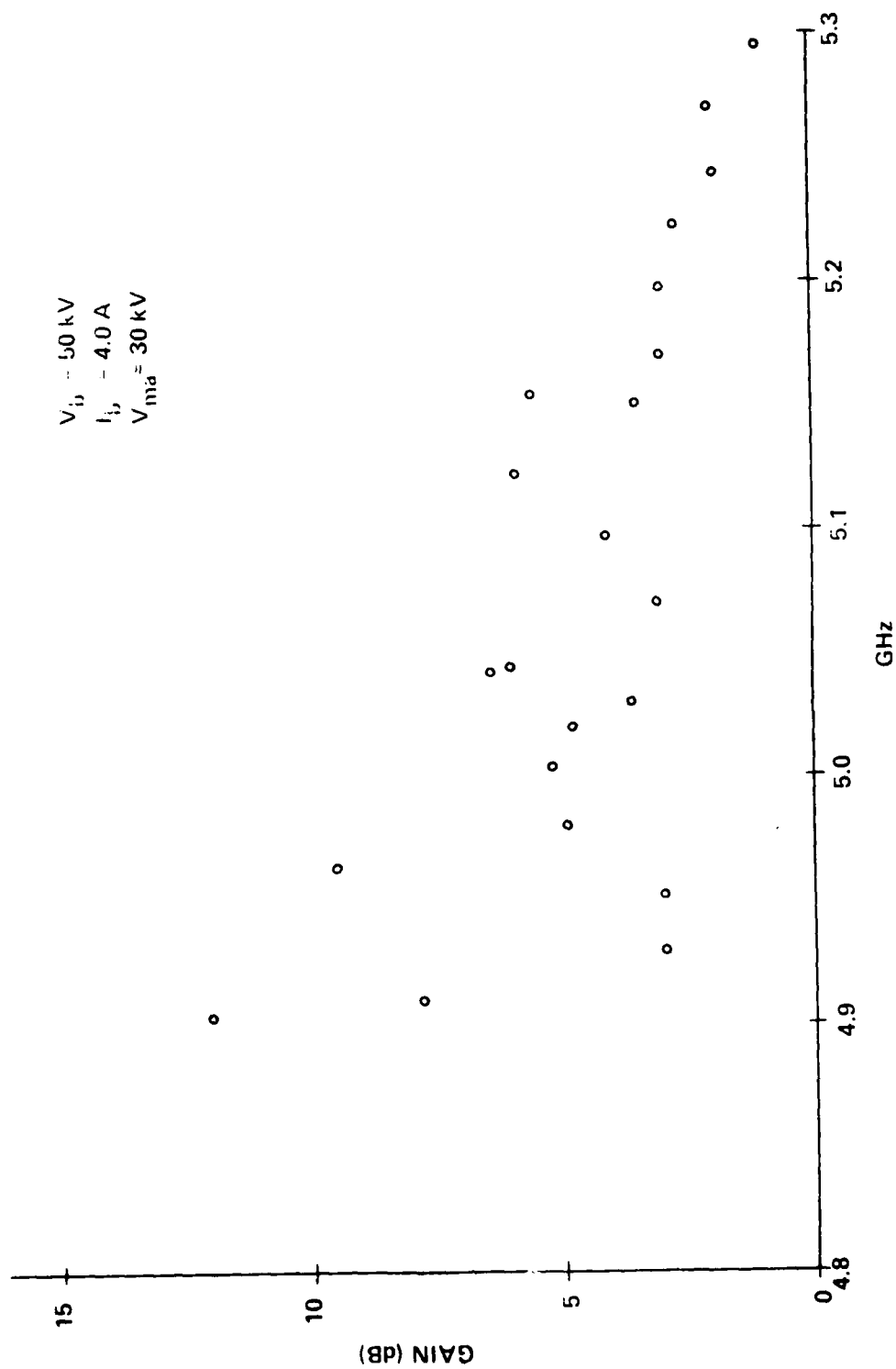


Figure 16. Gain vs Frequency for VGC-8160 S/N 1R1

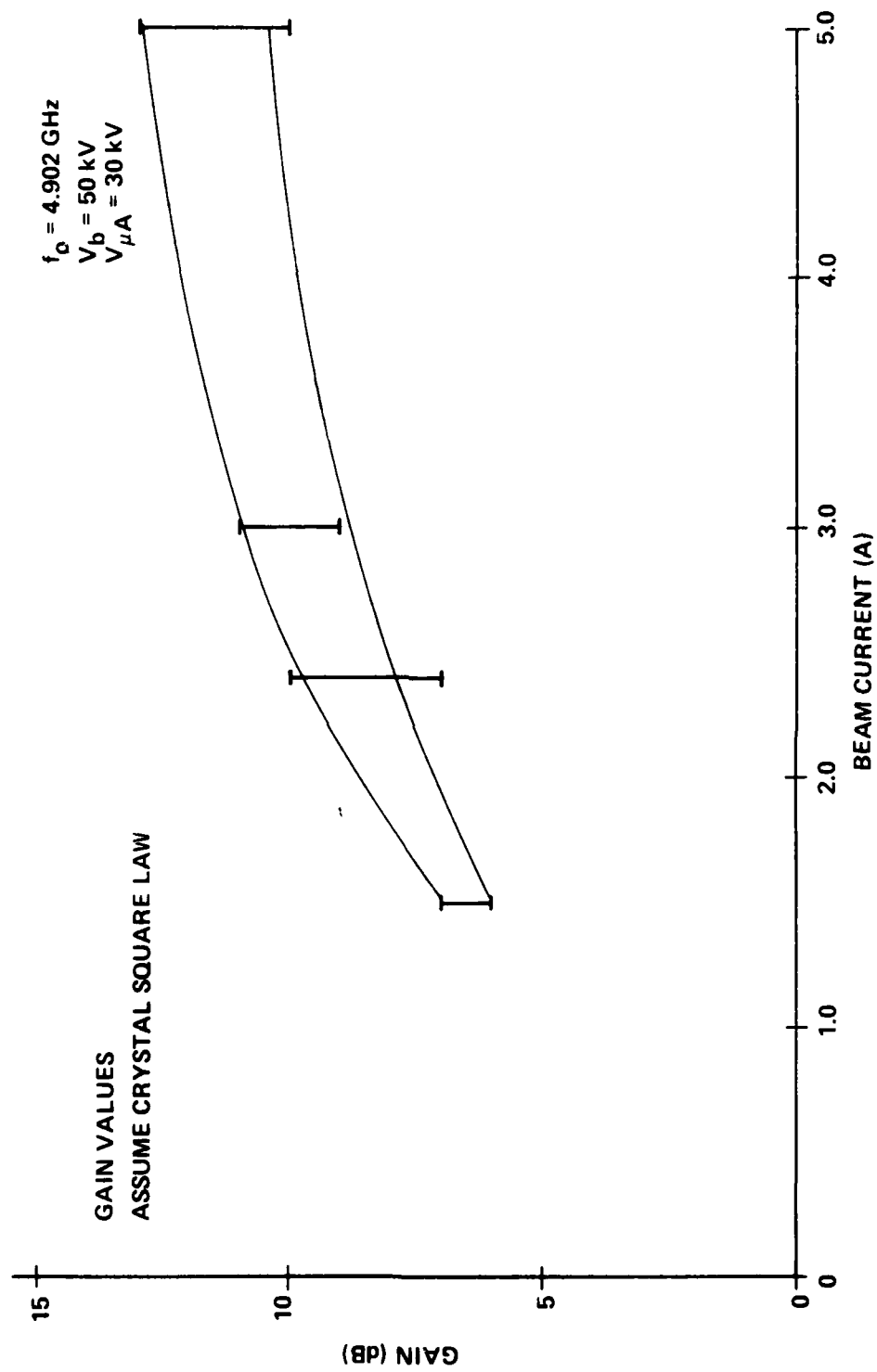


Figure 17. Gain vs Beam Current for VGC-8160 S/N 1R1

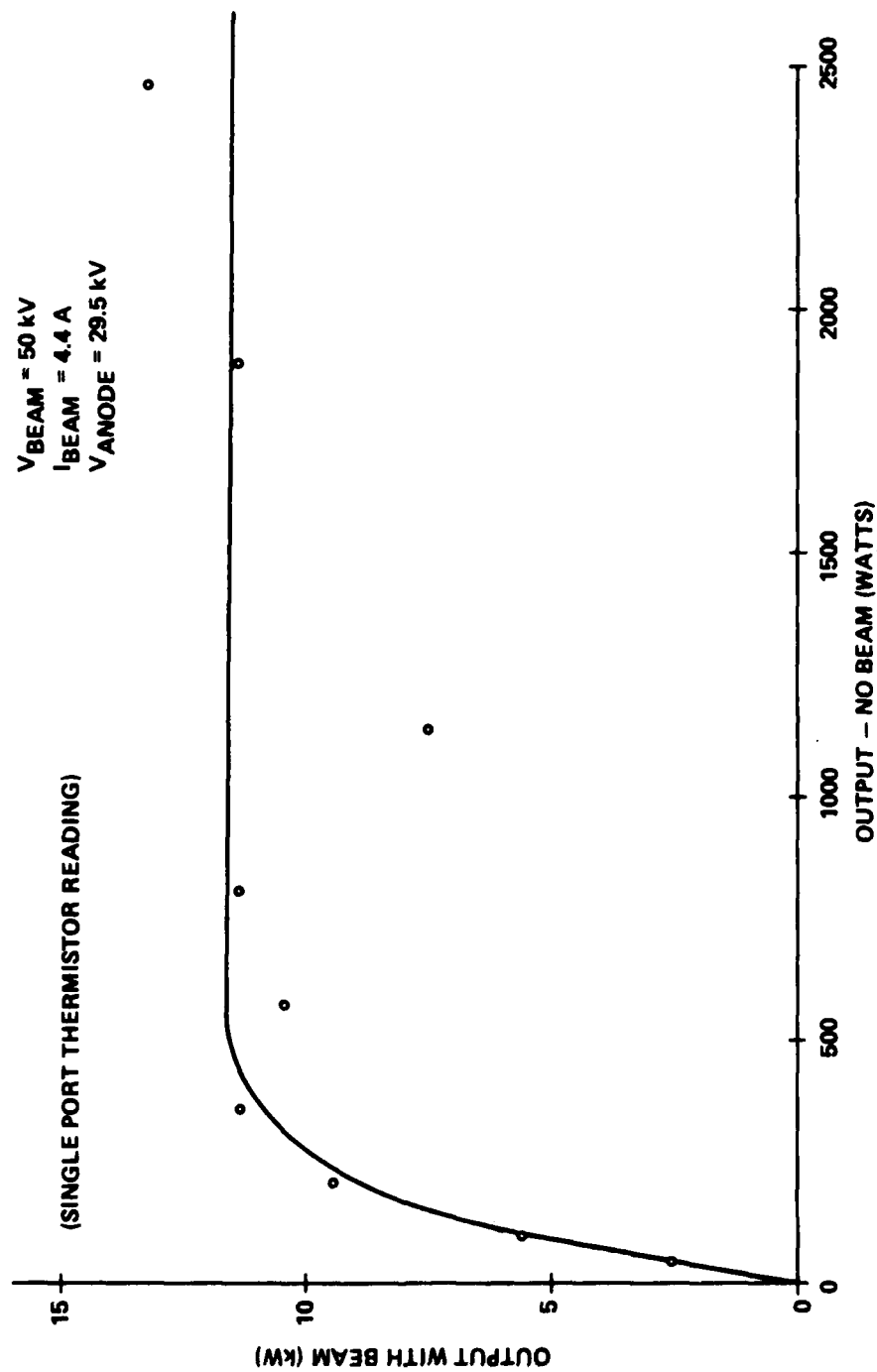


Figure 18. Output with Beam vs Output Without Beam VGC-8160 S/N 1R

C. SECOND REBUILD AND TEST OF THE GYRO-TWT: VGC-8160, S/N 1R2

The VGC-8160 S/N 1R1 was difficult to operate since the most interesting regions of operation occurred on the ragged edge of oscillation. It was decided to rebuild the tube with some effort made to stabilize the rf behavior.

One of the main contributors to the oscillatory behavior was clearly the difference between the operating range of the tube and the range of low VSWR for the input and output. Therefore, the rf circuit was rebuilt with tapers at the input and output so that the main section of circuit has a reduced diameter. This shifted the tube's operation into the region of good input and output match. In addition, the input transitions were redesigned around a simple rectangular to circular waveguide match. This was possible due to the use of the larger bore of the longer magnet. These transitions gave a much improved match as shown in Figure 19.

In order to improve stability, 6-10 dB of loss was added to the circuit. This loss was distributed evenly over the first two-thirds of the circuit. A cross section of the gyro-TWT is shown in Figure 20.

The tube was tested extensively. The best performance is listed in Table 7. The saturated gain is 6 dB less than the small signal gain similar to a linear-beam type traveling wave tube. The power out, bandwidth and electronic efficiency as listed are the best values published to date. Figure 21 shows the measured small signal gain compared to the gain calculated for a ratio of perpendicular to parallel momentum of 1.5. The small signal gain calculations are discussed later in this report. In the calculations, a launching loss of 9 dB was assumed. An additional launching loss of 3 dB was also subtracted. This loss occurred because only one drive line was excited and so half of the drive power went into a circularly polarized wave rotating in the wrong direction. An additional 3 dB was subtracted to allow for circuit loss. Saturated power output as a function of frequency is shown in Figure 22. The 3 dB saturated power bandwidth is 6%. The data in Figures 20 and 21 were taken without any adjustment of parameters.

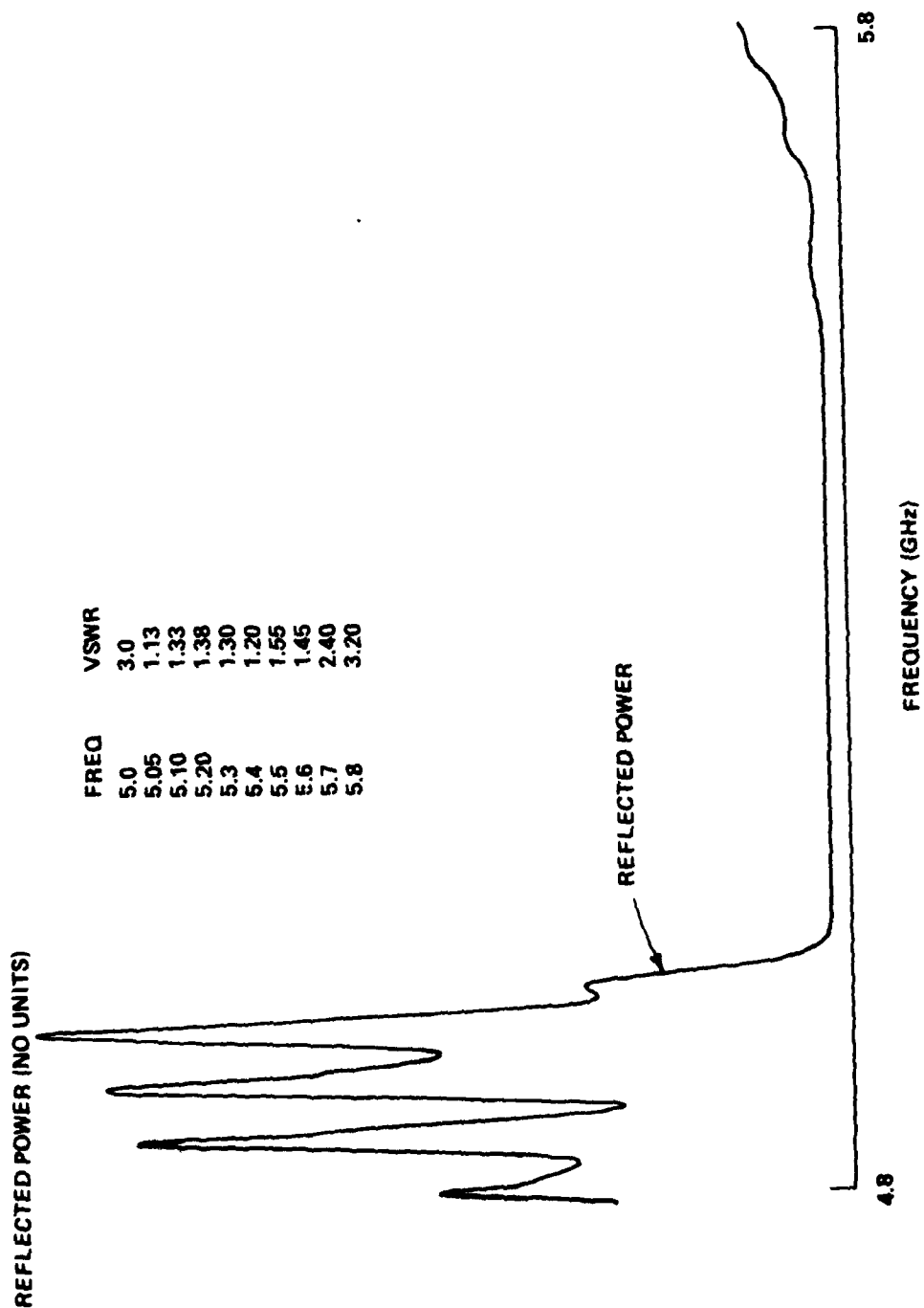


Figure 19. VGC-8160 Reflected Power Input Transition

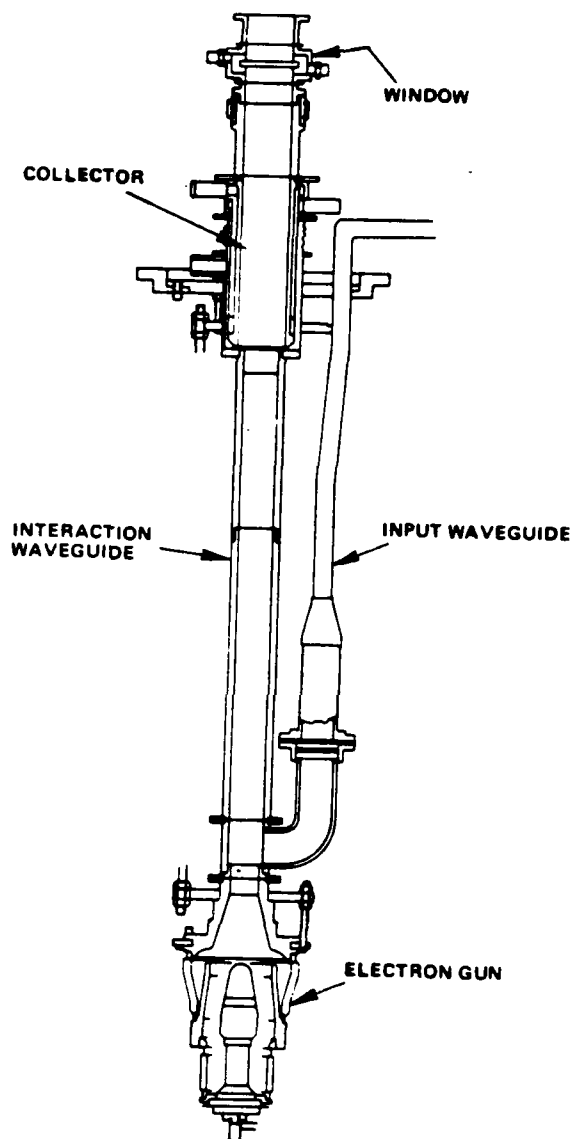


Figure 20. Gyro-TWT VGC-8160 S/N 1R2

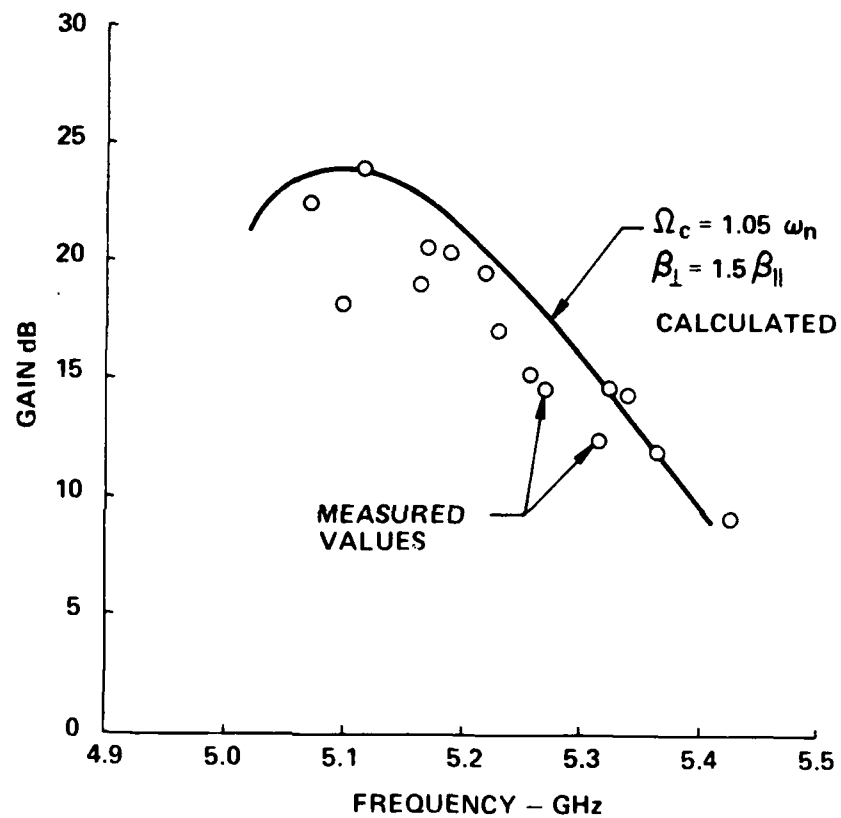


Figure 21. Comparison of Calculated and Measured Gain

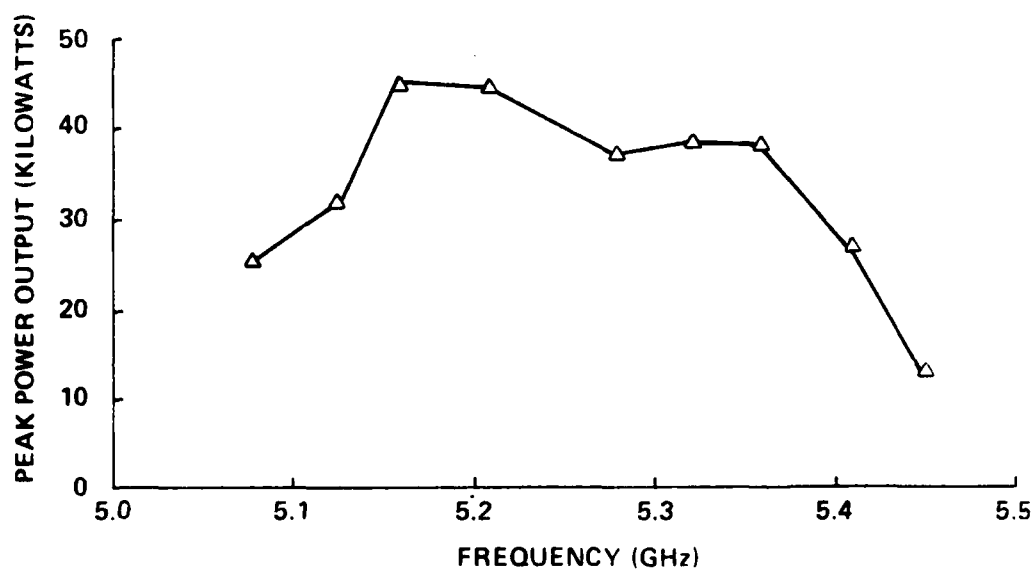


Figure 22. Saturated Power Output

TABLE 7
Performance of the Gyro-TWT, VGC-8160, S/N 1R2

Gyro-TWT (5.2 GHz)

Beam Voltage	60 kV
Beam Current	5 A
Power Output	50 kW
Small Signal Gain	24 dB
Saturated Gain	18 dB
Bandwidth (Saturated)	6% (3 dB points)
Electronic Efficiency	16.6%

D. SECOND HARMONIC TEST - VGC-8160 S/N 1R2

Power measurements at the second harmonic of the cyclotron frequency were performed on the gyro-TWT. All magnetic fields were reduced by 1/2 to allow operation at the fundamental frequency of 2.6 GHz. The rf frequency was set at 5.2 GHz, i.e., the second harmonic. Before applying voltages to the tube, the output power was measured very carefully from $f = 5.05$ GHz to 5.52 GHz. Then the beam parameters were adjusted to the values which yielded good gain and power out at the cyclotron frequency of 5.2 GHz. It was found that beam transmission was less than 50% with the reduced magnetic field. No second harmonic power was detected. The gun magnetic field was increased in several increments with $\pm 25\%$ variation in the main magnetic field at each increment until the beam transmission was greater than 90%. At each increment, rf power out was monitored. No amplification at the second harmonic was detected.

4. SMALL SIGNAL GAIN CALCULATIONS

The gyro-TWT, as stated in Section 3, was designed to employ the dominant TE_{11} mode in a circular waveguide.

There are at least two good reasons for building a gyro-TWT using a dominant waveguide mode and, in addition, there is a third reason for using the circular waveguide TE_{11}^0 degenerate dominant mode pair.

Studies of the dispersion relation for gyro-TWTs indicate that once the beam line intersects the waveguide dispersion hyperbola for a particular mode there will be gain in that mode, even if the cyclotron frequency is substantially above the cutoff frequency. Hence, a higher order waveguide mode gyro-TWT is almost certain to amplify in lower order waveguide modes if these modes are excited by structure or beam asymmetries. Second, the smaller the waveguide cross section, the higher will be the electric fields for a given power flow. Since the degree of bunching and the power removed from the beam are each a function of the electric field, then, as in a conventional traveling wave tube, the gain parameter will be greater if the electric field is produced by a small power flow than if it is produced by a large one.

A waveguide mode which exists as an orthogonal degenerate pair is desirable in a gyro-TWT because the electrons are orbiting and can interact continuously if they are in a circularly polarized field. One can think of the circularly polarized TE_{11}^0 mode as being made of the two degenerate linearly polarized TE_{11}^0 modes excited in space and time quadrature. If a certain power flow in one of the modes produces a certain field, and this power is then divided between the two orthogonal modes, the field of each mode will be $1/\sqrt{2}$ times as large. As a result, an orbiting electron will experience an interaction with the E_x and E_y field components (equivalent to the circularly polarized TE_{11}^0 mode) of magnitude $1/\sqrt{2} + 1/\sqrt{2} = \sqrt{2}$ times as large as that it would in a guide containing a single linearly polarized mode with the same power flow. The interaction impedance is proportional to

$\langle E \rangle^2 / P$ in which $\langle E \rangle$ is the time average of the electric field and P is the power flow in the waveguide. The impedance is therefore twice as large for circular polarization as for linear polarization.

The above conclusions were based upon inferences drawn from dispersion relations calculated by various authors (2-6) for other beam-waveguide geometries. Recently, however, Chu, Drobot, Szu and Sprangle (7) have published the dispersion relation for this specific geometry. With a little algebra it is possible to give the mode coupling factor in their equation a striking resemblance to Pierce's C^3 . That is

$$\bar{\omega}^2 - (\bar{k}^2 + 1) = - \frac{1}{4\pi^2 \beta_{\parallel}} G_b Z R \left\{ \beta^2 \frac{(\bar{\omega}^2 - \bar{k}^2)}{(\bar{\omega} - \bar{k}\beta_{\parallel} - s\bar{\Omega})^2} - \frac{(\bar{\omega} - \bar{k}\beta_{\parallel}) Q_{sm}}{(\bar{\omega} - \bar{k}\beta_{\parallel} - s\bar{\Omega}) H_{sm}} \right\} \quad (2)$$

in which $\bar{\Omega} = \Omega/\omega_n$, $\bar{\omega} = \omega/\omega_n$, $\bar{k} = k/k_n$, Ω is the electron cyclotron frequency, ω is the operating frequency, ω_n is the waveguide cutoff frequency, and k_n is the normal wavenumber which is equal to ω_n/c . G_b is the dc beam conductance equal to the beam current, I_b , divided by the beam voltage, V_b , β_{\parallel} and β are the axial and transverse beam velocities normalized with respect of the velocity of light, and

$$R = [V_b/V_n] / [1 + V_b/V_n] \quad (3)$$

in which $V_n = mc^2/e = 511,000$ volts is a measure of the rest mass energy. The factor R is the efficiency with which energy modulation is turned into angular velocity modulation. (This is analogous to the factor of 1/2 which comes from the square root relation between electron velocity and electron energy in conventional linear beam tubes.) The circuit impedance Z for TE_{mn}^o modes is given by

$$Z = \frac{4\pi^2 \eta_1 H_{sm}(x,y)}{\pi x_{mn}^2 K_{mn}} = \frac{(\lambda_n E)^2 v_g}{2P c} \quad (4)$$

in which η_1 is the characteristic impedance of free space and H_{sm} , which is related primarily to the integral of the tangential electric field on the electron around its orbit, is given by

$$H_{sm}(x,y) = [J_{s-m}(x) J'_s(y)]^2. \quad (5)$$

As shown above, Z can be thought of as the ratio of the square of the normalized strength, $\lambda_n E$, of the multipole component of the electric field (which is responsible for interaction at the harmonic s) divided by the power flow P and normalized with respect to the ratio of c to v_g , the group velocity of the unperturbed waveguide mode (λ_n is the free-space wavelength at the waveguide cutoff frequency).

The factor Q_{sm} which arises primarily out of the radial forces of the multipole fields on the orbiting electrons results in damping. This is given by

$$Q_{sm}(x,y) = 2 H_{sm}(x,y) + y \left[J_{s-m}^2(x) J'_s(y) J''_s(y) \right. \\ \left. + \frac{1}{2} J_{s-m-1}^2(x) J'_s(y) J'_{s-1}(y) - \frac{1}{2} J_{s-m+1}^2(x) J'_s(y) J_{s+1}(y) \right] \quad (6)$$

and K_{mn} which relates to the power flow in the waveguide is given by

$$K_{mn} = J_m^2(x_{mn}) - J_{m-1}(x_{mn}) J_{m+1}(x_{mn}) \quad (7)$$

In the above expressions $x_{mn} = k_n r_w$, $x = k_n r_o$ and $y = k_n r_c$ in which r_w is the waveguide radius, r_o is the hollow beam radius (i.e., the radius of the cylinder which is the locus of the guiding centers of the electrons) and r_c is the cyclotron radius.

The roots of equation (1) give the propagation characteristics of the growing wave

$$H_z = H_{z0} \exp \left[j(\omega_r t - kz) + \omega_i t \right] \quad \text{or} \\ H_z = H_{z0} \exp \left[j(\omega t - k_r z) + k_i z \right] \quad (8)$$

in which ω_r and ω_i are the real and imaginary parts of a complex ω solved for as a function of real wavenumber, k , and k_r and k_i are the real and imaginary parts of a complex wavenumber solved for as a function of real frequency. It does not matter much how one solves the equation because the temporal growth rate ω_i is related simply to the spatial growth rate k_i by the relationship

$$k_i = \omega_i \left(\frac{\partial \omega_r}{\partial k} \right)^{-1} = \omega_i / v_g \quad (9)$$

In this case v_g is the group velocity of the unstable wave.

Figure 23 shows the normalized frequency ω_r/ω_n and the normalized temporal growth rate ω_i/ω_n as functions of normalized wavenumber k/k_n . Figure 24 shows the gain in dB/cm derived from the spatial growth rate, k_i , as a function of frequency for the parameters we used in the experimental tubes we built and for electrons with a perpendicular momentum 1.5 times the parallel momentum. From our gun calculations we believe this momentum ratio is close to the experimental values.



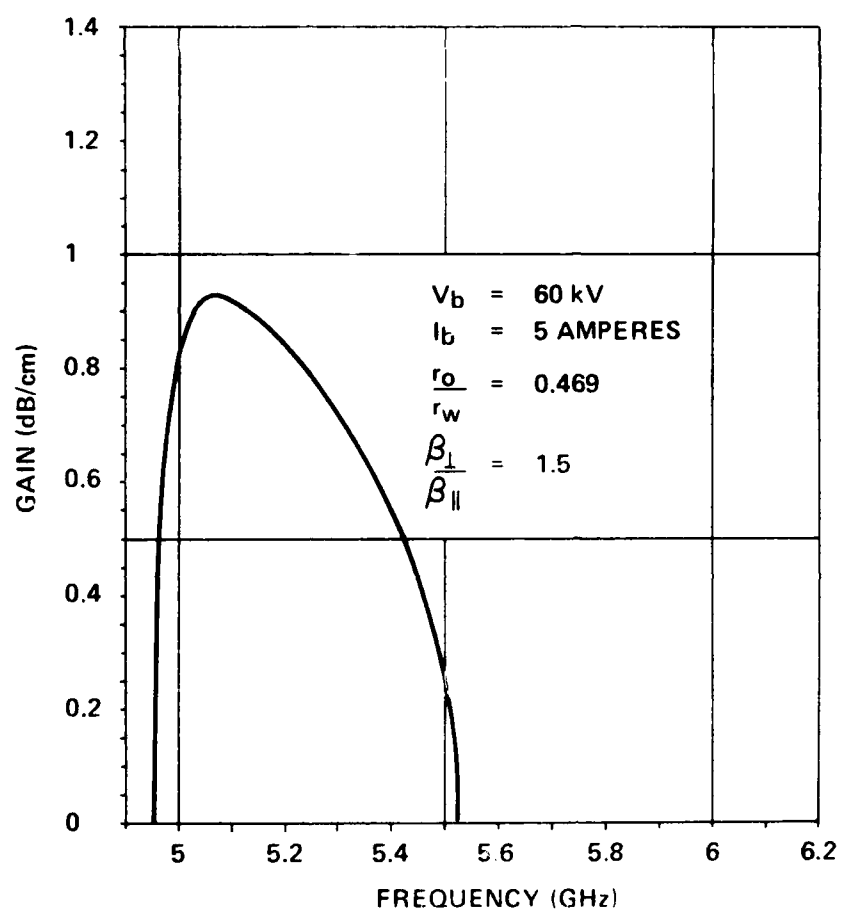


Figure 24. Calculated Gain in dB/cm vs Frequency

5. HIGH IMPEDANCE CIRCUIT CALCULATIONS

A. INTRODUCTION

The strength of the interaction in a gyro-TWT depends upon the circuit impedance in much the same way as in a conventional TWT. This circuit impedance is proportional to the ratio of the square of the transverse electric field seen by the beam to the power flow in the guide. One obvious way of obtaining a high circuit impedance is to operate in the dominant waveguide mode as we have done in our present experimental tube. Another way is to use a rectangular or ridged waveguide so the electric field is not strong outside the region occupied by the electron beam. It also seems logical that the impedance of the circuit could be increased by restricting the bandwidth. There is a possibility that this might widen the frequency range over which synchronism is achieved and improve the hot bandwidth of gyro-TWTs. We recognize that the use of periodic circuits would remove one of the attractions of gyro-TWTs; that is, the use of large simple circuits. However, if the dimensions can be kept large enough and the performance potential is interesting enough, the use of periodic circuits may be justifiable. We have therefore made some computations to determine the feasibility of the use of such circuits in gyro-TWTs.

B. PREDICTIONS

The calculations which will be described were made for a parallel-strip transmission line. However, the analytical work will be presented so as to permit the results to apply also to a rectangular or a ridged rectangular waveguide. Figure 25(a) indicates a succession of narrow slits, each cut so as to introduce a series inductance into the transmission line. Figure 25(b) indicates a widening of the slits to about half the period of the loading. Figure 25(c) indicates that the slots have been enlarged further so that only thin partitions remain. In all cases, an increase in transverse impedance occurs at the center of the region between the inductances, i.e., where the metal conductors approach one another most closely. (A longitudinal impedance develops at the position of an inductance, hence the transverse impedance is diminished there.) Of course,

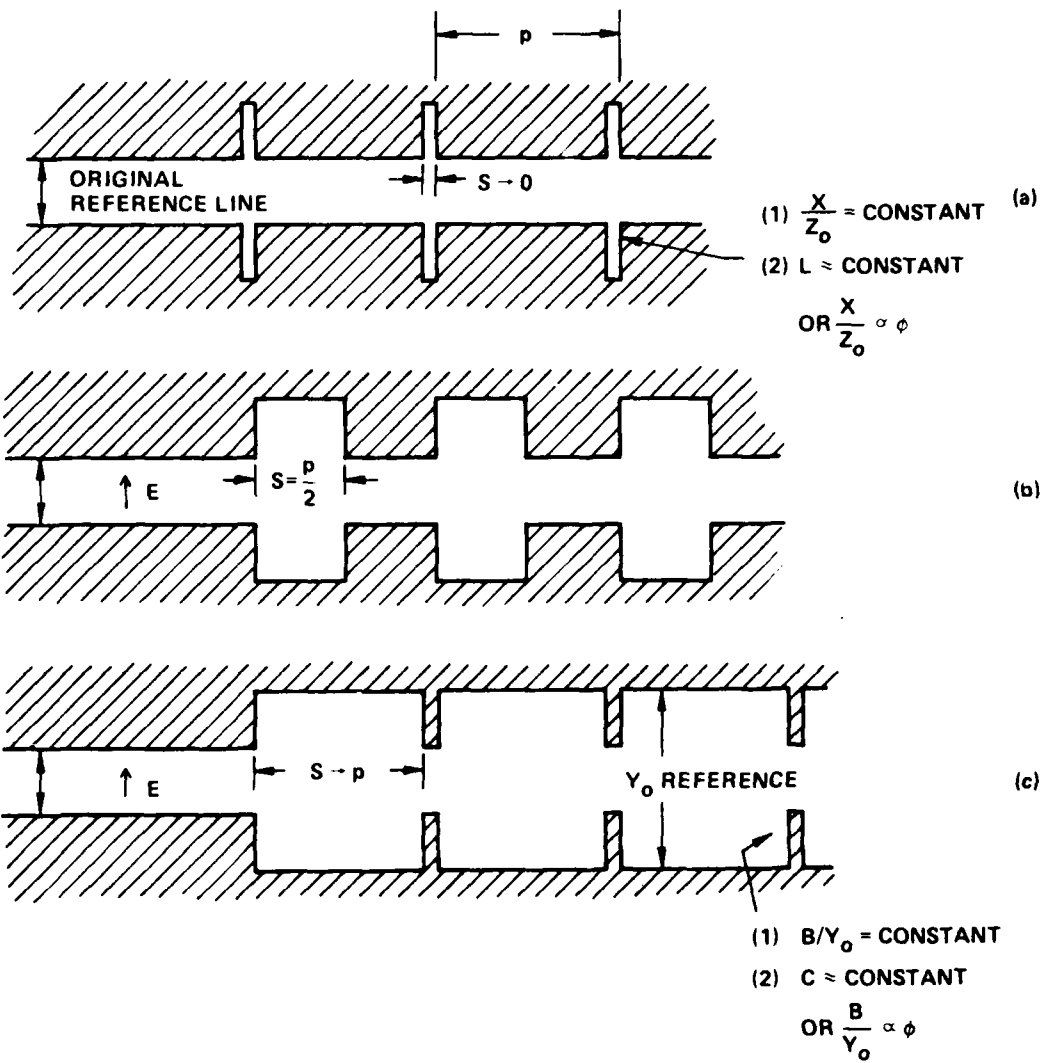


Figure 25. Transmission Line with Periodic Loading and Increase Transverse Impedance

the periodic alterations of the original transmission line produce a low-pass filter (overlooking any lower cutoff if a waveguide is used), hence the effects of interest occur at frequencies close to the upper edge of the filter passband.

The case of Figure 25(a) is analyzed as a transmission line for which $Z_0 \equiv 1/Y_0 = 1$, with localized series loading reactances, X . Two subcases are considered. In Case 1, we assume $X/Z_0 \equiv x = \text{a fixed constant}$ -- a good approximation over a narrow frequency range not too close to any possible slot resonance frequency. In case 2, we assume $x = h\phi$, where h is a design constant and ϕ is the electrical length of the transmission line between loading points. For TEM-mode propagation on the line, ϕ is linear with frequency, hence $x \propto \omega$ here. This is a viable assumption when the physical slot is narrow and not deep enough to produce a slot resonance near any frequency of interest. In a closed waveguide, ϕ will increase with increasing ω , though not linearly except when ω is well above the waveguide cutoff frequency. The overall phase shift per period is defined as θ . The analytical methods used are well known in circuit analysis and need not be detailed here.

Figure 26 is essentially a Brillouin diagram, except that the ordinate is ϕ rather than ω . Figure 26 applies to the case of Figure 25(a) with normalized $x = \text{constant} = 0, 0.5, 1, 2, 4$. With increasing x , narrowing of passbands and widening of stopbands is observed. Of course, the curves are now accurate for very small values of ϕ since the assumption $X/Z_0 = \text{constant}$ must break down in reality as $\omega \rightarrow 0$. For completeness, an upper passband for the system is shown ($\phi > 180^\circ$); its relevance is subject to the degree of validity of the assumption $X/Z_0 = \text{constant}$ over the frequency range involved.

Figure 27 plots Y/Y_0 vs ϕ for the case at hand, and for the plane midway between loading elements. Whenever $Y/Y_0 < 1$, the transverse impedance has been increased, as desired.

From Figure 27, it is seen that the transverse impedance approaches infinity as ϕ approaches the value for which cutoff ($\theta = 180^\circ$) occurs

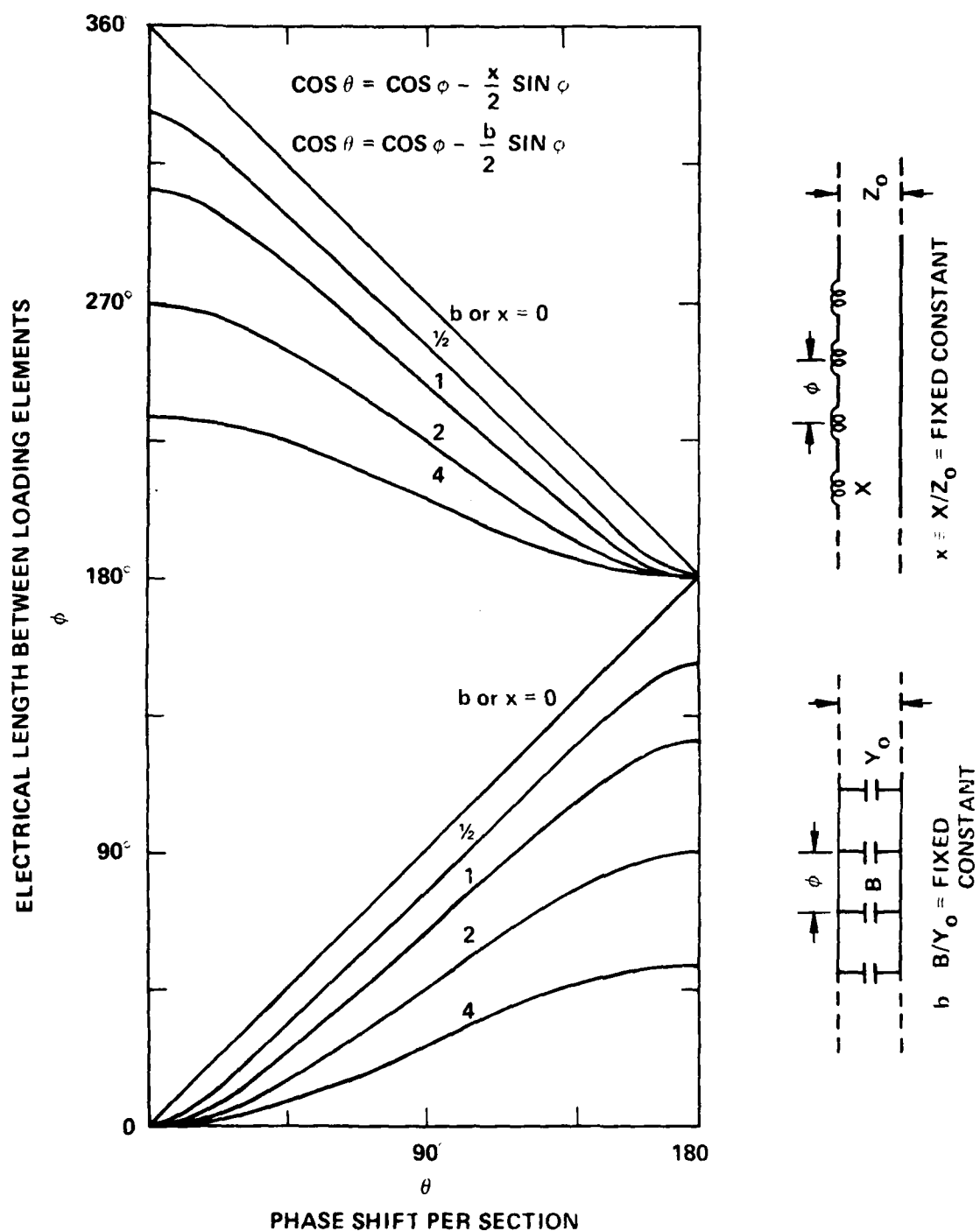


Figure 26. Brillouin-Type Diagram for Transmission Line with Periodic Loading by Either Lumped Series Inductances or Shunt Capacitances; Case 1, constant ratio of B to Y_0 or X to Z_0

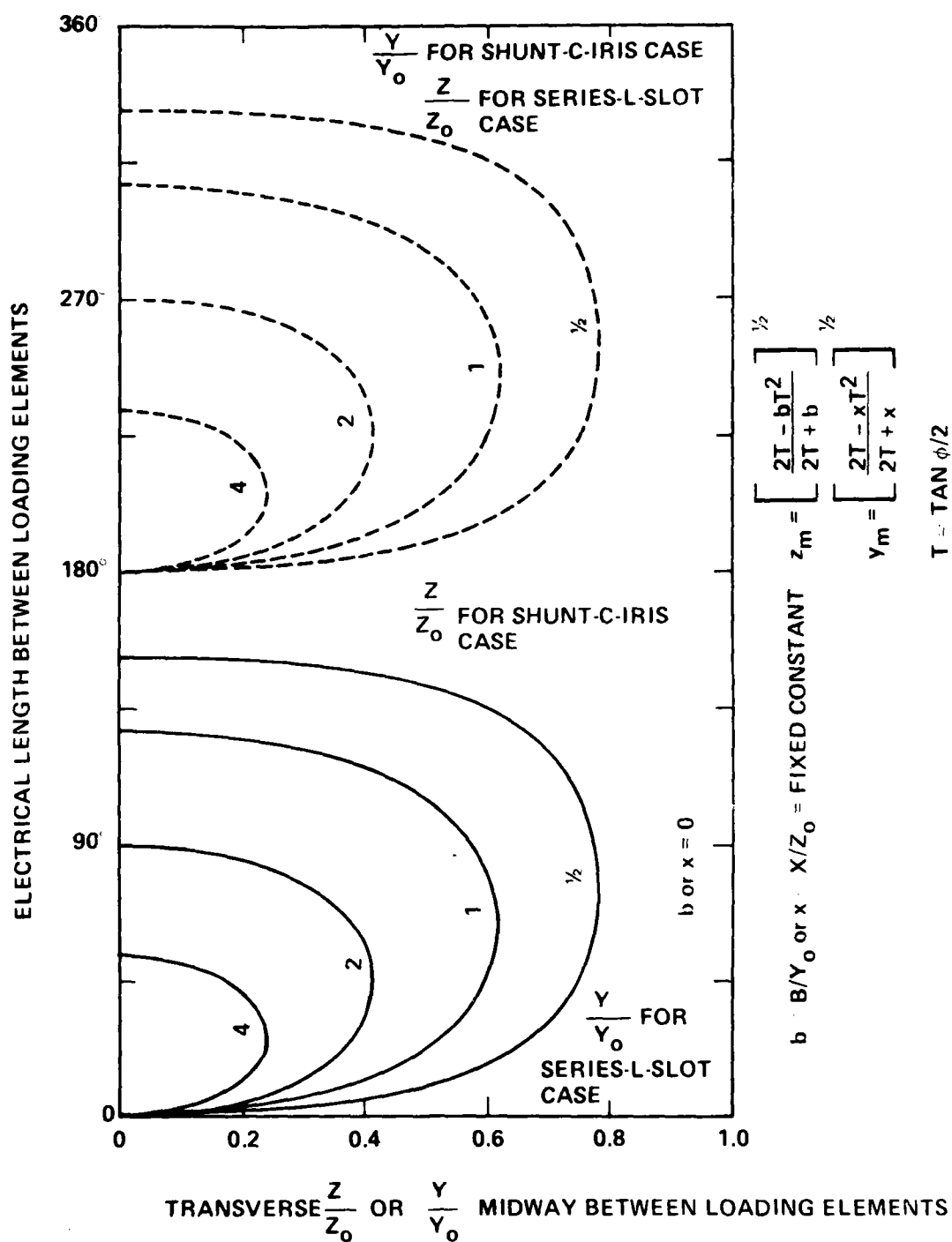


Figure 27. Normalized Transverse Impedance or Admittance Predictions for Case of Figure 26, Evaluated Midway Between Loading Elements

according to the chosen value of X/Z_0 . Of course, the approach of the transverse impedance to infinity at low values of ϕ should be ignored; this is a consequence of the assumption $X/Z_0 = \text{constant}$ regardless of frequency. We note that in the upper passband ($180^\circ < \phi < 360^\circ$) the transverse impedance is decreased, in planes midway between loading elements, less the addition of such elements. (This result is, of course, contingent on the validity of the assumption regarding X/Z_0 .)

If the decrease in transverse impedance in a plane containing the loading element is of interest, Figure 28 is to be consulted. Ignoring the low- ϕ tail of each curve (for reasons stated previously), the transverse impedance decrease in the plane of a loading element, and the increase in the plane midway between elements, are in an approximately reciprocal relationship. (The net effect on electrons remains to be evaluated.)

Figures 29, 30, and 31 apply for the model of Figure 25(a), Case 2, $x = X/Z_0 = h\phi$. The quasi-Brillouin diagram of Figure 29 shows the narrowing of the passband with increasing h (the constant of proportionality between X/Z_0 and ϕ). These curves are "well behaved" for $\phi \rightarrow 0$.

As expected, Figure 30 shows that, in a plane midway between loading elements, the transverse impedance approaches infinity as ϕ approaches the value for which $\theta = 180^\circ$ (edge of passband), according to the chosen value of h . Figure 31 applies to the plane of the loading element. Again, the transverse impedance decrease in such a plane is approximately the reciprocal of the increase occurring in a plane midway between the series-inductive loads.

Figures 32 and 33 cover the case of Figure 25(b), which is essentially a corrugated waveguide. The waveguide sections between steps are each $\phi/2$ long electrically and alternately have the impedances $Z_{01} = 1$ and $Z_{02} = A$; the basis of impedance normalization is the Z_0 of the sections having the closer spacing between conductors. All fringing capacitances have been neglected. Figure 32 indicates that a low-pass filter has again been produced. At the center of a section where the conductors are closest, we see (Figure 33) that the transverse impedance always exceeds the value prior

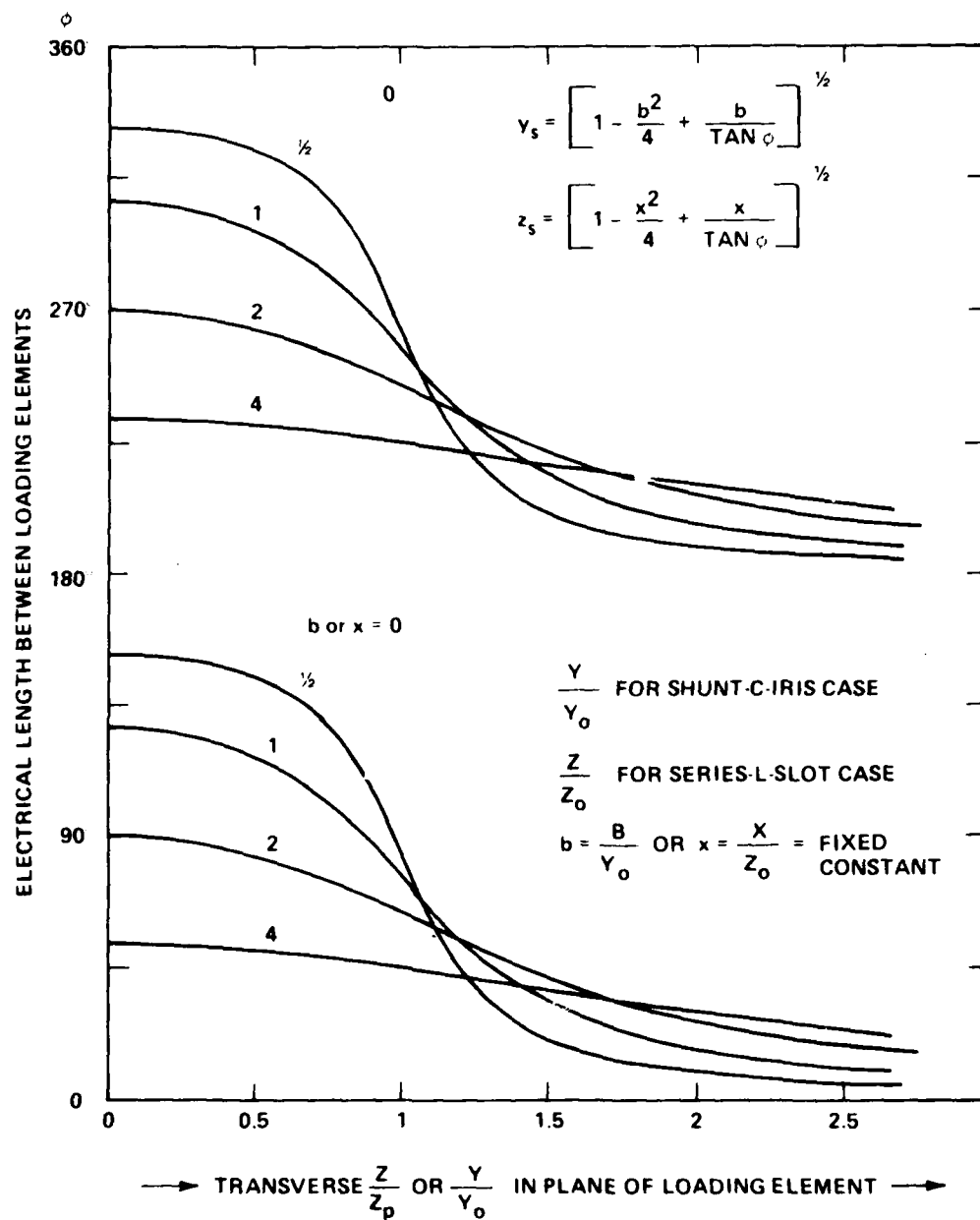
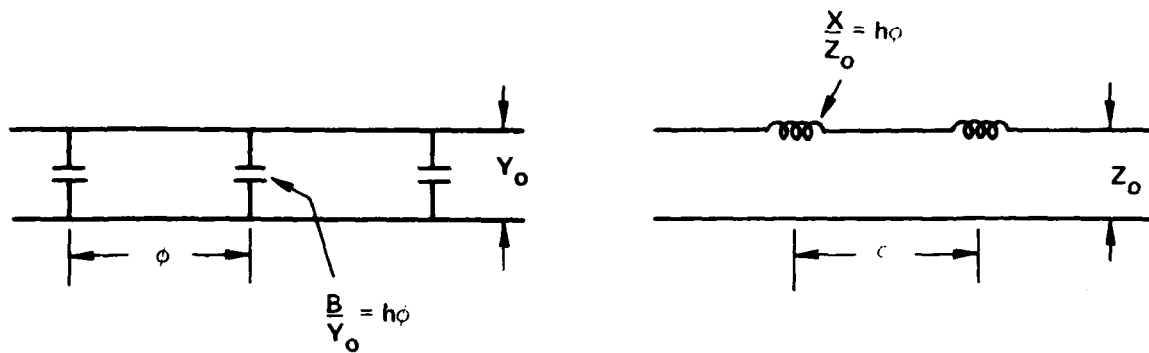


Figure 28. Normalized Transverse Impedance or Admittance Predictions for Case of Figure 26, Evaluated in Plane of Loading Element



$$\cos \theta = \cos \phi - \frac{h\phi}{2} \sin \phi$$

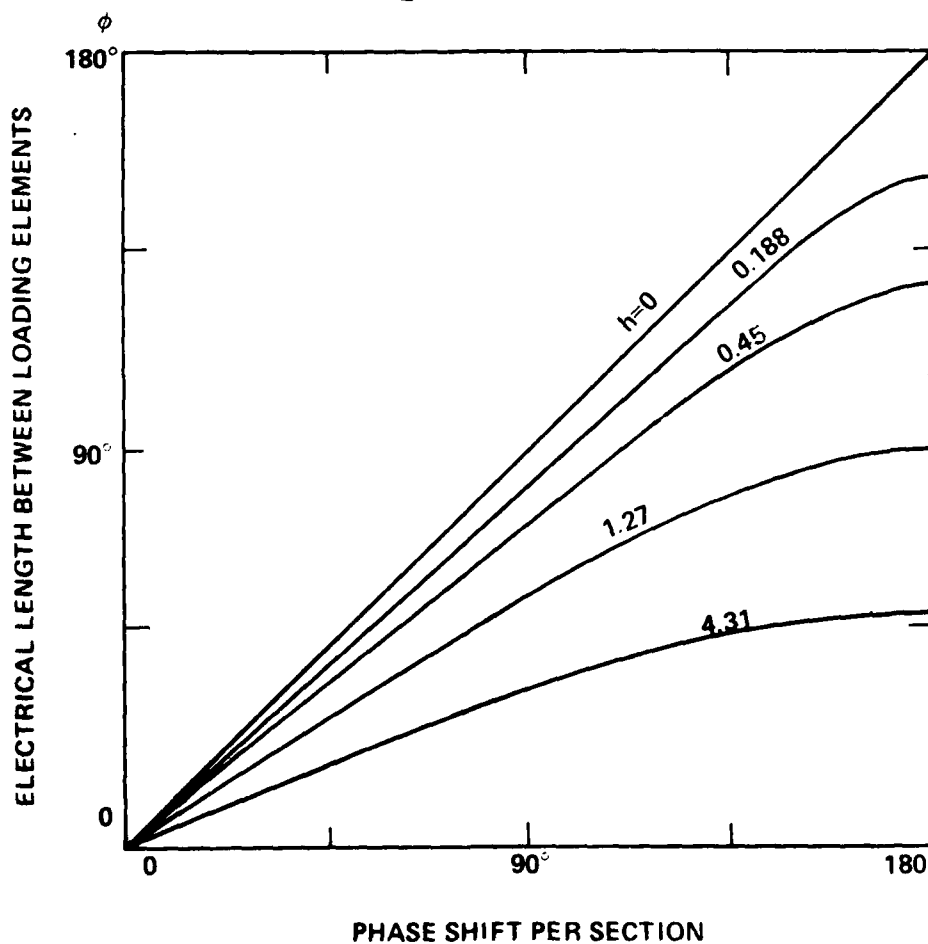


Figure 29. Brillouin-Type Diagram for Transmission Line with Periodic Loading by Either Lumped Series Inductances or Shunt Capacitances; Case 2, ratio B/Y_0 or X/Y_0 is Proportional to Electrical Length ϕ

$$z_m \text{ or } y_m = \left[\frac{2T - h\phi T^2}{2T + h\phi} \right]^{\frac{1}{2}}$$

$$\text{where } T = \tan \phi/2$$

$$\frac{\beta}{Y_0} \text{ or } \frac{X}{Z_0} = h\phi$$

$$\frac{Z}{Z_0} \text{ FOR SHUNT-C-IRIS CASE}$$

$$\frac{Y}{Y_0} \text{ FOR SERIES-L-SLOT CASE}$$

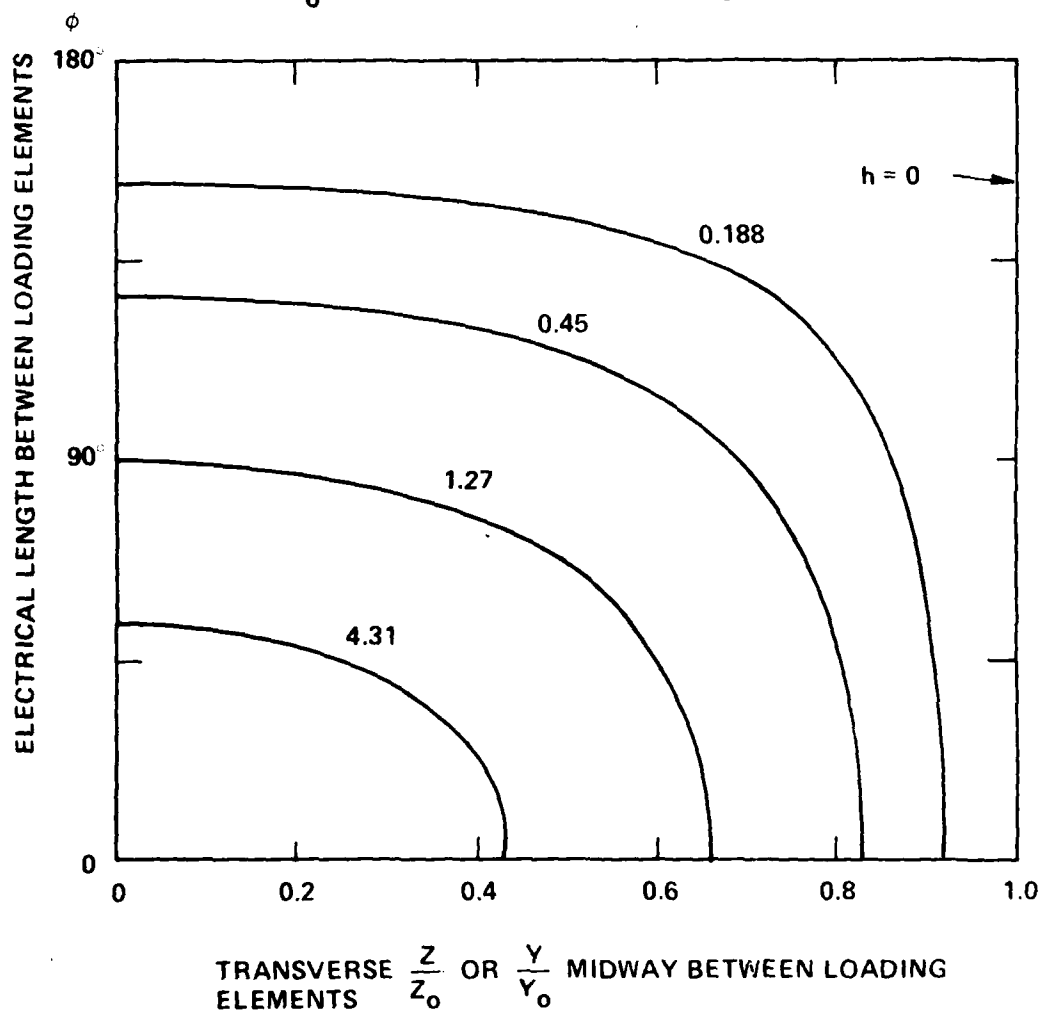


Figure 30. Normalized Transverse Impedance or Admittance Predictions for Case of Figure 29, Evaluated Midway Between Loading Elements

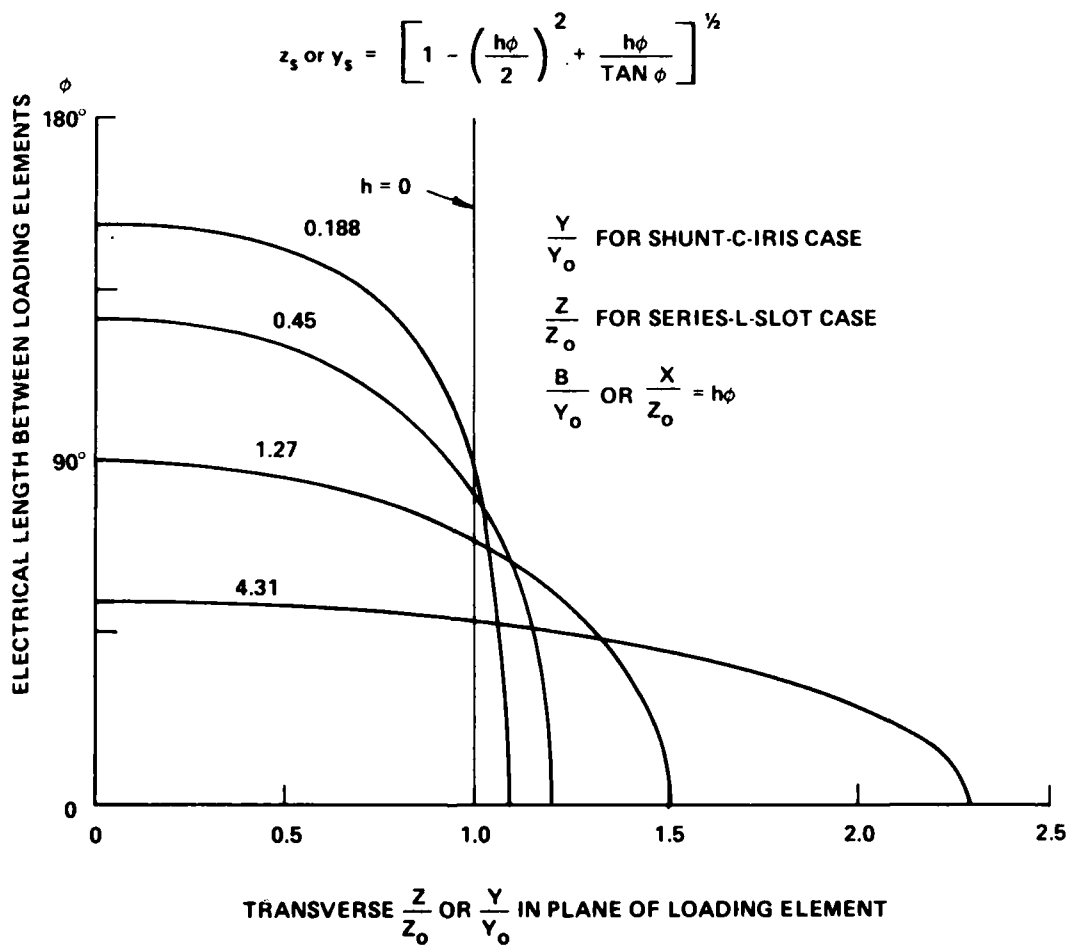


Figure 31. Normalized Transverse Impedance or Admittance Predictions for Case of Figure 29, Evaluated in Plane of Loading Element

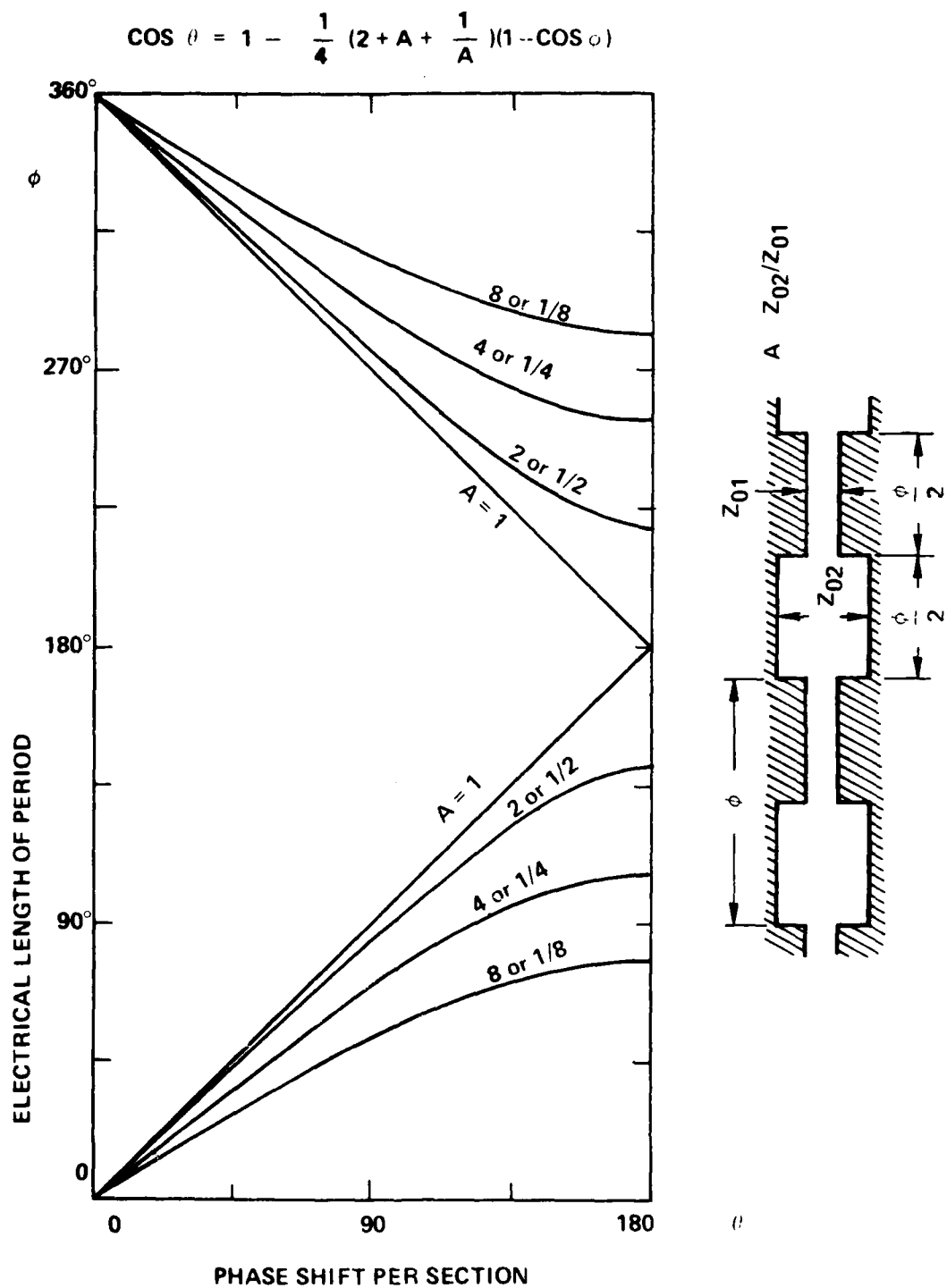


Figure 32. Brillouin-Type Diagram for Corrugated Transmission Line

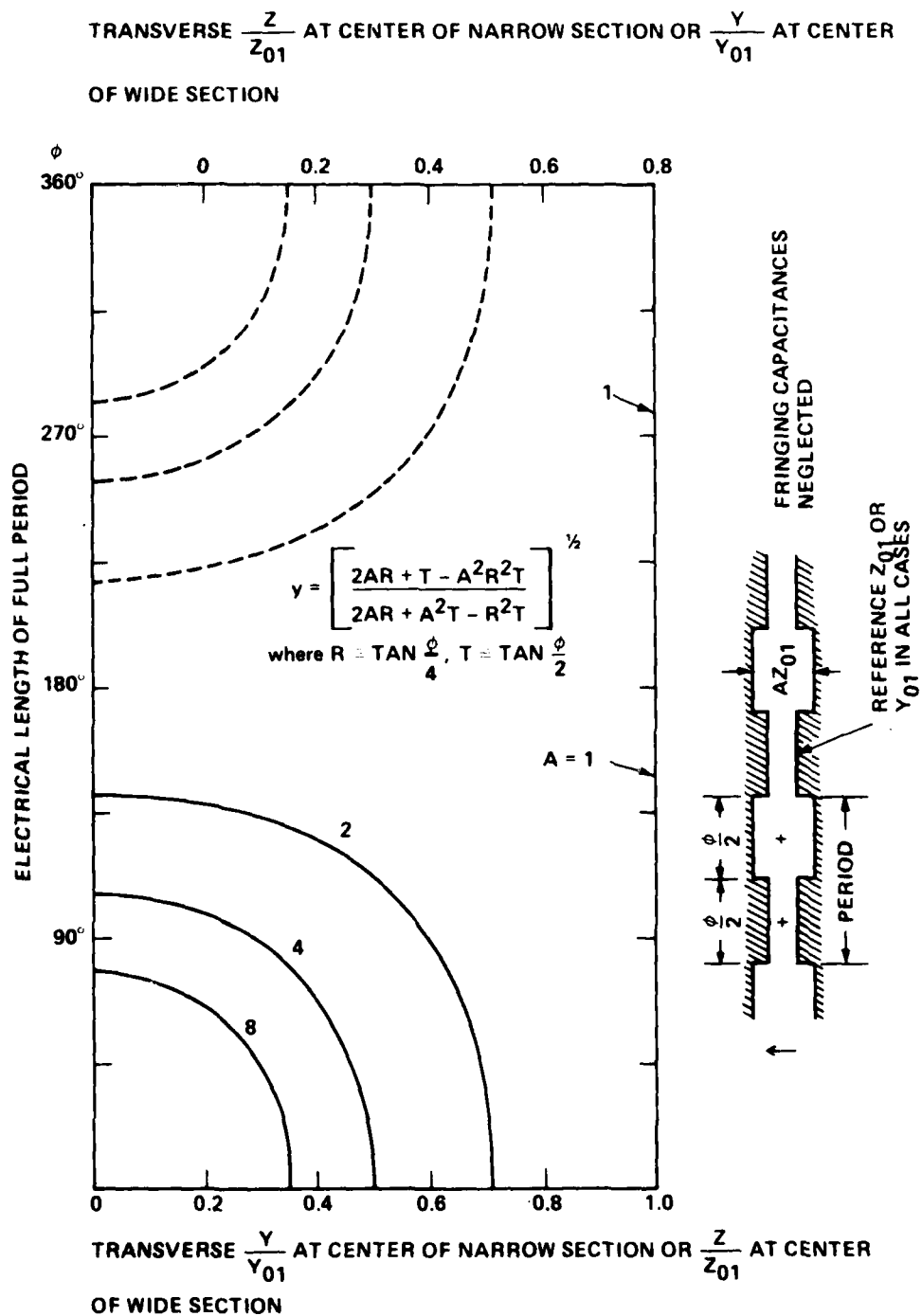


Figure 33. Normalized Transverse Impedance or Admittance Predictions for Case of Figure 32

to corrugating (Z_{01}) and approaches infinity at the upper edge of the passband. The more disparate the two waveguide heights (parameter A), the narrower the passband and the greater the enhancement of transverse impedance. However, at the center of a section where the conductors are furthest apart, the transverse impedance is decreased by an exactly reciprocal amount.

For the case of Figure 25(c), the electrical behavior is describable by Figures 26-31, properly reinterpreted. Figure 25(c) gives a relatively wide-spaced transmission line (all impedances are now normalized to the Z_0 corresponding to the widest spacing) periodically loaded with shunt-capacitive irises with $b \equiv B/Y_0$. Again we have Case 1, $B/Y_0 = \text{a constant}$ (Figures 26, 27, 28), or Case 2, $B/Y_0 = h\phi$ (Figures 29, 30, 31). As expected, the transverse impedance tends to be increased in the plane of the capacitive iris and decreased, roughly reciprocally, in planes midway between irises. Of course, these values of transverse impedance are all relative to a Z_0 that was high to begin with; this fact would be taken into account when predicting electronic interaction.

C. CONCLUSIONS

Although some simplifying assumptions have been made, we have generated models for estimating the trends of transverse-impedance change, and its variation with frequency, resulting from corrugating a transmission line, inserting localized series-inductive slots, or introducing localized shunt-capacitive irises. Basically, the transverse impedance rises in a plane where the conductors come closest together, and falls where the conductors move apart -- all relative to the Z_0 of the unloaded transmission line. The overall effect on electrons gyrating and drifting through the line remains to be evaluated.

D. IMPLEMENTATION

We visualize a double-ridged rectangular waveguide, with the electron beam passing down the gap between the two ridges. The ridges will be serrated, according to Figure 25(a) or (b) or (c), as appropriate. Since

the lowest cutoff frequency can be very low here, we view this as a two-strip transmission line with periodic loading.

Alternatively, we can work with a simple TE_{10} rectangular waveguide. Series inductive stubs can be built onto the broad walls of the guide. Interestingly, it would suffice to simply cut transverse slots in the broad walls, or slots tilted at 45° in the narrow walls. Since the waves inside are slowed, such slots will not radiate at frequencies below that for which the slot length is a half wavelength.

In a TE_{on} guide (circular electric), the cutting of rows of slots all over the pipe surface, with all slots fitted about 45° , produces velocity slowing as is appropriate to the insertion of periodic series inductance. The phenomena here are well behaved (without radiation) at frequencies below that corresponding to a slot resonance.

6. GYRO-TWT GUN AND MAGNET DESIGNS

A. GUN DESIGNS

Two design approaches were followed for the electron gun to be used on the 94 GHz gyro-TWT. The two approaches are: (1) the conventional magnetron gun and (2) the Pierce-type gun with a helically-varying transverse magnetic field. The design goals were:

Beam Voltage	60 kV
Beam Current	5 A
Beam Diameter	0.041 in
Velocity Ratio (v_{\perp}/v_{\parallel})	1.5

The majority of the gun design effort in the last several months has been directed toward the Pierce-type gun with a bifilar helix and accompanying magnetic circuit. As reported in a recent monthly report, close monitoring was maintained on the magnetron gun design procedure for a 28 GHz and a 110 GHz gyrotron program. It is considered that the methods by which these guns have been designed can be applied in a straightforward manner to a gun to be operated at 94 GHz. The following discussion on magnetron guns is concerned with these methods.

B. MAGNETRON GUN

Recent successes in the construction and test of magnetron guns on the 28 GHz gyrotron program for electron cyclotron heating in plasmas indicate that the basic design techniques have been established at Varian.

The careful consideration of cathode loading and space charge effects resulted in a successful 28 GHz gyrotron gun that used a cathode that was short in relation to its mean diameter and a cathode half-angle of approximately 10° . Also the 28 GHz gun design used a relatively low magnetic field in the cathode region, which allows the cyclotron wavelength of the electrons to be large with respect to the cathode length. This in

turn allows the electrons to pass through similar fields in order to attain a similar energy distribution and a lower velocity spread.

Scaling of the successful 28 GHz gun to higher frequencies presented several problems. The desire to minimize space charge effects, the need for higher magnetic fields in the interaction region and the necessity of maintaining approximately the same beam compression ratio all contributed to a higher magnetic field in the gun region. The higher magnetic field decreases the cyclotron frequency, which makes it more difficult to cause all electrons in the beam to experience the same electrostatic and magnetostatic forces. In addition, decreasing the cathode mean diameter while maintaining reasonable current density caused the cathode to become considerably longer with respect to the mean diameter. These problems led to a re-evaluation of certain design constraints.

Recently published calculations [10,11] indicated that increasing the cathode half-angle from 10° to 25° would make significant progress in providing the desired electron flow. This analysis was performed by the method of analytic continuation, in which a desired electron flow was assumed and the necessary boundary conditions were determined. In addition, it was recognized that more freedom in adjusting the fringing fields was allowable, provided that the magnetic fields employed were "real", i.e., producible by means of a coil system. With these two major changes in the design approach, a very promising magnetron gun design was achieved for a 110 GHz gyrotron development [9]. The parameters for that design were as follows:

Beam Voltage	80 kV
Beam Current	8 A
Cathode Loading	5 A/cm ²
Cathode Half-angle	23°

Figures 34, 35 and 36 show computer simulation of representative electron trajectories for that design for three different lengths of the front focus

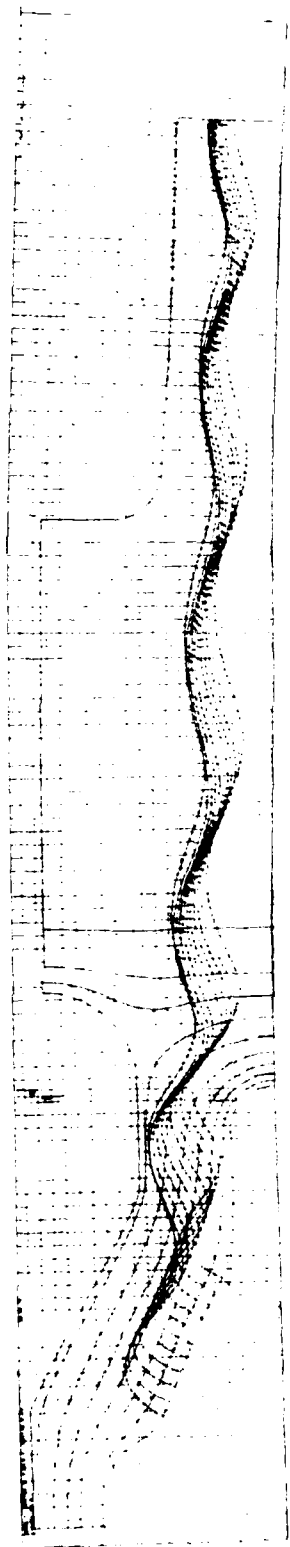


Figure 34. Electron Trajectories for a Twenty-Three Degree Cathode Angle with a Short Front Focus Electrode

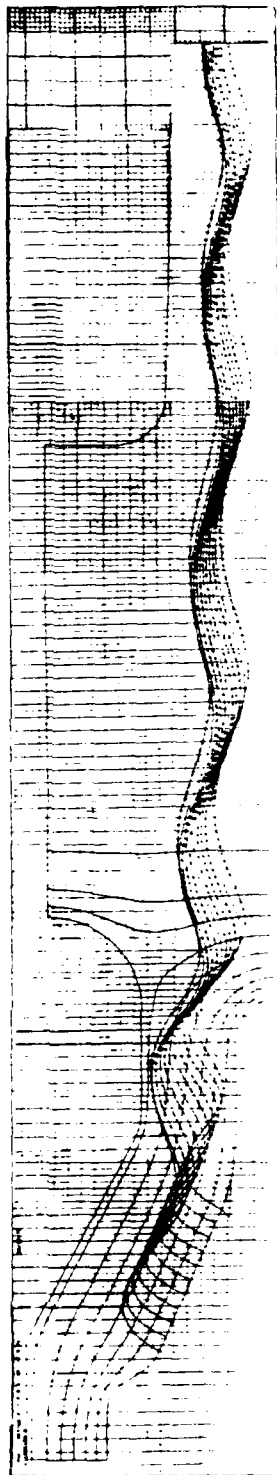


Figure 35. Electron Trajectories for a Twenty-Three Degree Cathode Angle with a Medium Front Focus Electrode

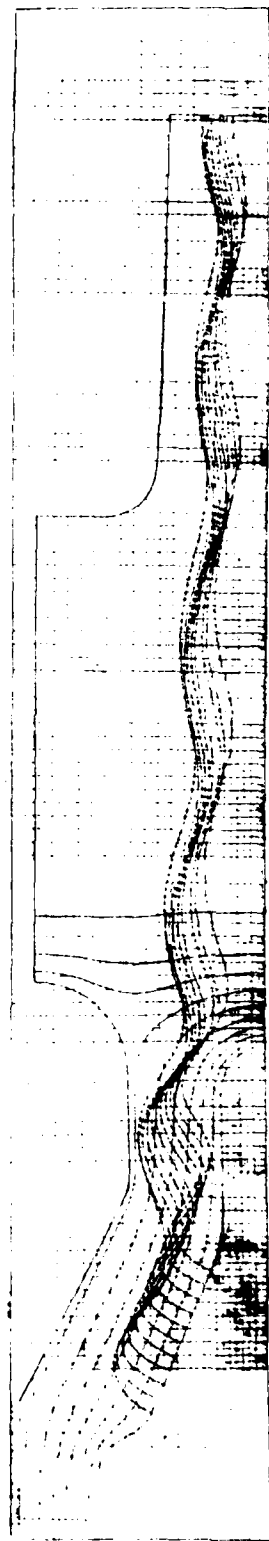


Figure 36. Electron Trajectories for a Twenty-Three Degree Cathode Angle with a Long Front Focus Electrode

electrode. Mean transverse energy normalized to total electron energy and velocity variation for the three front focus electrodes are listed in Table 8.

Table 8
Transverse Energy and Velocity Spread for Three Gun Designs

Front Focus Electrode	Mean Transverse Energy/Total Energy	Velocity Variation
Short	0.929	$\pm 6.80\%$
Medium	0.772	5.40%
Long	0.598	3.25%

The simulation yielding the best velocity variation ($\pm 2.1\%$) with 5 A/cm² cathode loading and mean transverse energy to total energy ratio of 0.811 is shown in Figure 37. At the time of this report efforts were continuing to reduce the cathode loading below 3.5 A/cm² to ensure long life while maintaining the velocity variation to less than $\pm 2.5\%$. With a slight modification of parameters this gun design should be usable for the proposed 94 GHz gyro TWT.

C. PIERCE-TYPE ELECTRON GUN WITH TRANSVERSE MAGNETIC FIELD

In the previous sections, a gyro-TWT exhibiting reasonable rf power, efficiency, gain and bandwidth was demonstrated. However, agreement has not been obtained between predicted and measured efficiency. Recent publications^{7,12} have predicted performance with efficiency as high as 51% with 2.0 dB/cm gain for 2.6% bandwidth, and 22% efficiency with 4.6 dB/cm gain for 11% bandwidth. The first example was optimized for maximum efficiency and the second example for maximum gain. These calculations were based upon zero electron momentum spread, i.e., $\Delta\beta_{\perp}/\beta_{\parallel} = \Delta\beta_{\parallel}/\beta_{\parallel} = 0$. Fair agreement was obtained between theory and experiment when the electron momentum spread was assumed to be 15%¹². It is considered then that there is an inherent momentum spread in magnetron guns.

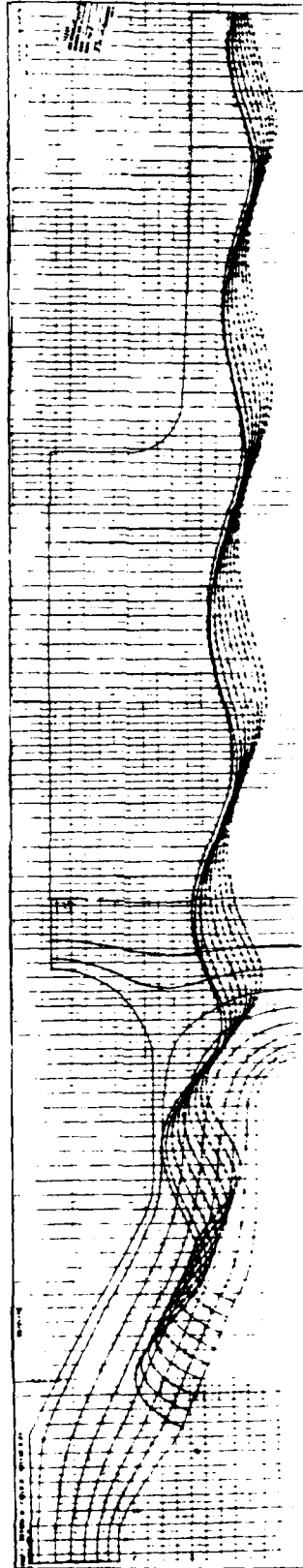


Figure 37. Electron Trajectories for a Five Ampere Per Square Centimeter Cathode Loading Design

A geometrical problem exists in scaling the existing 5 GHz gyro-TWT magnetron gun to 94 GHz. Because a small beam (0.043" dia.) is needed and the cathode must have an area large enough to support a current of 5 amperes, a large area convergence is required. The large convergence makes it difficult to obtain an electron beam with the small spread in momentum needed for high efficiency.

These two reasons, i.e., the inherent momentum spread and the accentuation of the spread due to high area convergence, prompted the consideration of an alternate approach toward formation of an electron beam. The alternate approach utilizes a bifilar helix of a fixed length to produce a transverse magnetic momentum with less than 2% spread to a solid electron beam emanating from a Pierce-type electron gun. The electron beam, upon exiting the helical region, is adiabatically compressed, with an accompanying increase in transverse momentum in the rf interaction region. A schematic diagram is shown in Figure 38.

The desired ratio of perpendicular momentum to parallel momentum $\beta_{\perp 2}/\beta_{\parallel 2}$, as discussed earlier, in the region of the interaction circuit is 1.5. The ratio of $\beta_{\perp 1}/\beta_{\parallel 1}$ for the beam exiting the bifilar helix can be determined from the relation (Appendix)

$$\frac{\beta_{\perp 1}}{\beta_{\parallel 1}} = \left[\frac{1}{\left(\frac{r_1}{r_2}\right)^2 \left[\left(\frac{\beta_{\perp 2}}{\beta_{\parallel 2}}\right)^2 + 1 \right] - 1} \right]^{1/2}$$

where

r_1 = radius of electron beam in the bifilar helix region

r_2 = radius of electron beam in the interaction region

For $\beta_{\perp 2}/\beta_{\parallel 2} = 1.5$, $\beta_{\perp 1}/\beta_{\parallel 1} = 0.165$ for $r_2/r_1 = 5.0$ which gives an area convergence of 25:1.

It remains then to determine the helix length and transverse magnetic field which will give the required momentum ratio of 0.165. The helix length was determined by calculating electron trajectories of arbitrary

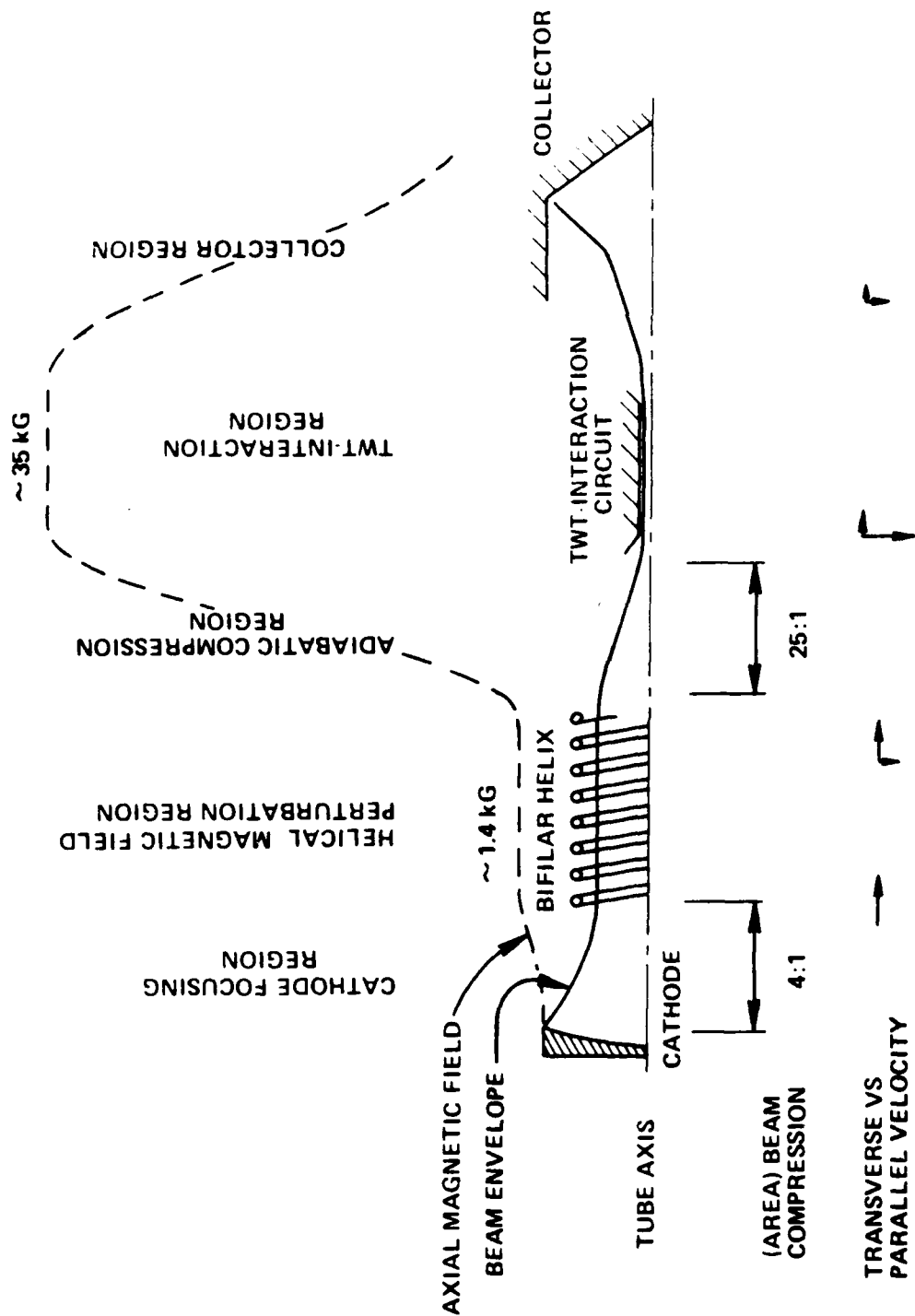


Figure 38. Schematic layout of 94 GHz Gyro-TWT using a Pierce-Type Gun

energies in an axial magnetic field, \vec{B}_0 , with the transverse magnetic field, \vec{B}_1 , superimposed upon \vec{B}_0 . The magnetic field \vec{B}_1 is given by

$$\vec{B}_1 = \hat{x} B_x + \hat{y} B_y$$

or

$$\vec{B}_1 = I_0(kr) [\hat{x} (\sin kz) + \hat{y} (\cos kz)]$$

where

\hat{x}, \hat{y} = unit vectors in the x, y direction

$I_0(kr)$ = Bessel function of zero order, first kind and imaginary argument

k = cyclotron wave number

z = axial distance

The program was parameterized to include the helix pitch in ratio with the electron cyclotron pitch. In Figure 39, the effect of B upon the electron beam is shown for a ratio of B_1/B_0 of 0.5%. The pitch of the helix is 5.0% longer than the cyclotron pitch of the electron. The three curves correspond to electrons at the center of the beam $kr = 0$, at the mid-radius ($kr = 0.25$) and at the edge ($kr = 0.5$). Note that at the normalized helix length $z = 36.5$, the momentum ratio of $\beta_{\perp 1}/\beta_{\parallel 1}$ is 0.165 with less than 1% spread. It is the uniqueness of employing a bifilar helix of an exact length and pitch to give a precise momentum ratio with very low spread that makes this approach very attractive. Earlier attempts^{11,12,13} at utilizing this approach did not realize this uniqueness.

D. MAGNETIC CIRCUIT DESIGN

The main focusing field necessary for operation of a gyro-TWT at 94 GHz is approximately 35.4 kilogauss. To avoid physical, electrical and material limitations it is preferable to form this field using a superconducting

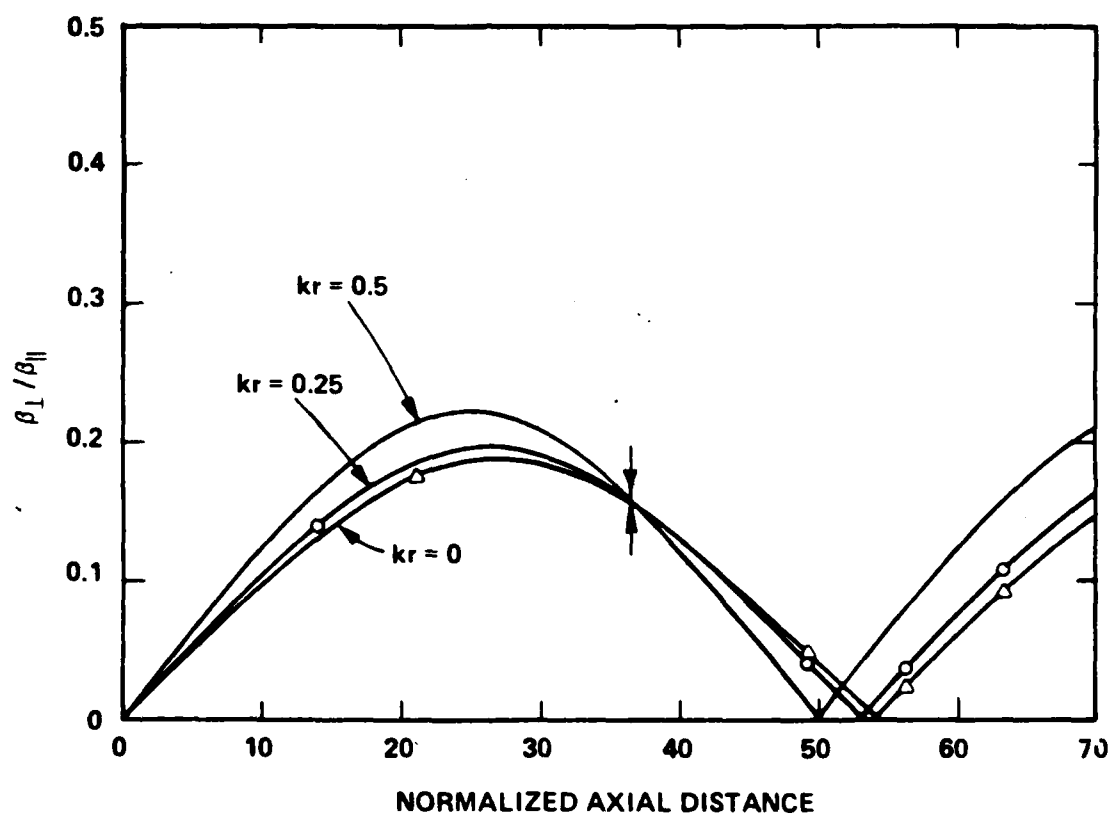


Figure 39. $\beta_{\perp}/\beta_{\parallel}$ vs Normalized Helix Length For Three Electron Rays For $B_{\perp}/B_0 = 0.5\%$

solenoid. This leads to the problem of maintaining a liquid helium environment, a problem that is minor compared to generating a 35.4 kilogauss field with a room temperature solenoid.

The dewar system that is used to cool the superconducting coil system puts a constraint on the minimum inside diameter of those coils. Because of this, the shape of the fringe field of the coil system providing the main focusing field may not be decreasing sufficiently and in the desired manner so as to form the beam from the gun system. A supplementary coil system is then needed to obtain the desired field shape. It would be most beneficial to have this supplementary coil system separate from the main focusing field system, and to have a more conventional non-superconducting solenoid providing the fringe field shaping. This room-temperature solenoid would be more adaptable to alteration; therefore, it was decided to investigate primarily this hybrid system. It was also recognized that the field for the Pierce-type gun system would be more complicated, since it was necessary to have two regions of uniform field, instead of one (as in the case of the magnetron injection gun system).

In light of these matters, a magnetic circuit for the Pierce gun system including the "corkscrew" or helical field region, was designed under the following approaches.

The question of obtaining the two regions of uniform field was investigated using a magnetostatic computer simulation program called NUTCRACKER (courtesy of Stanford Linear Accelerator Center). It has been implemented on the in-house computer at Varian and operates satisfactorily. This program takes into account the finite permeability of iron, and the nonlinear saturation effects. This program has demonstrated excellent agreement with existing, measured solenoid fields.

The question of obtaining the proper field shape in the cathode region for the 60 kV, 5 A, 4:1 area convergence Pierce-type gun was obtained with another in-house computer program at Varian. This program solves Laplace's equation in 2-dimensional cylindrical coordinates (R, Z). In this program, iterations were performed to investigate different polepiece shapes which

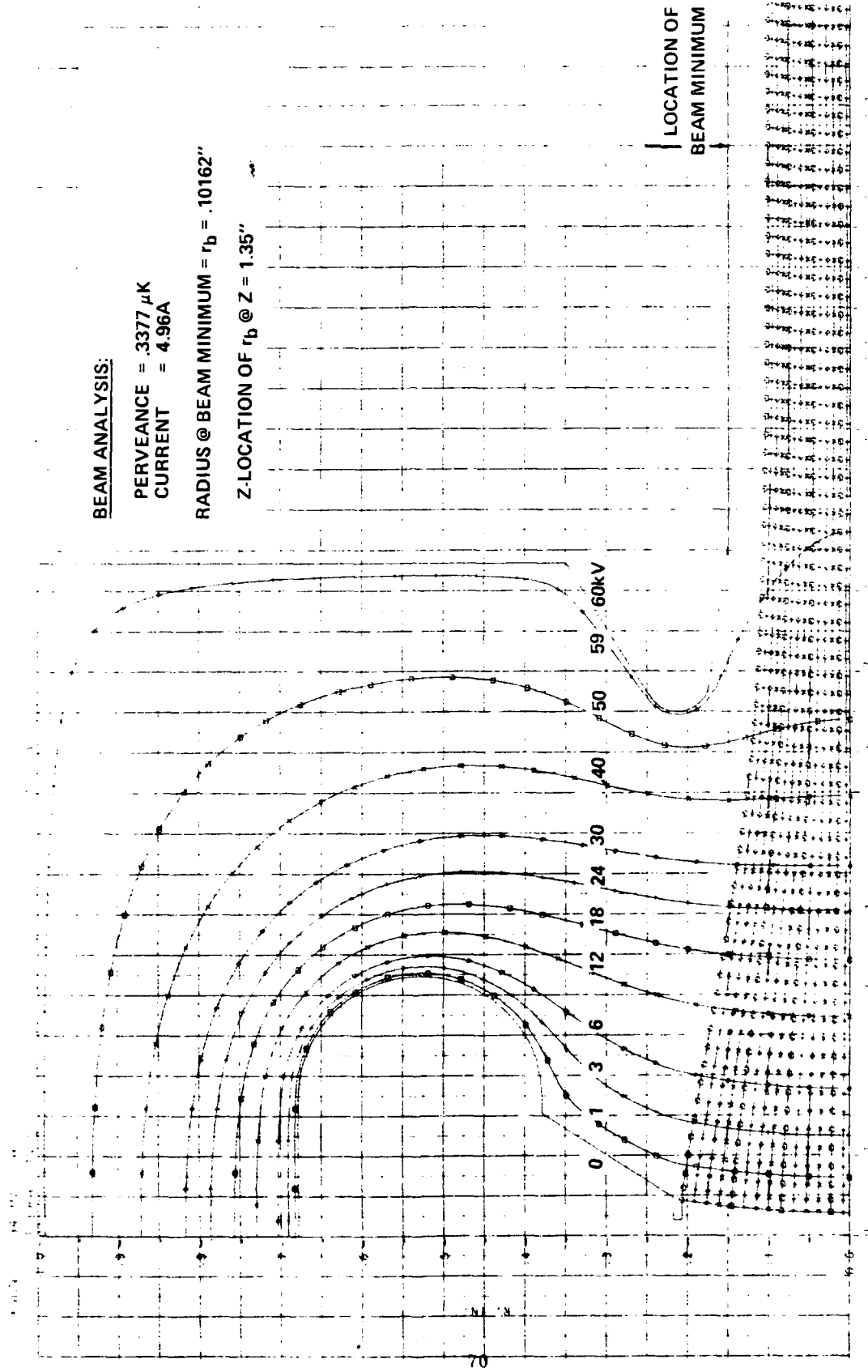


Figure 40. Computed Electron Trajectories For The Pierce-Type Diode Gun - Zero Magnetic Field

would provide a magnetic field that would induce a minimum of scalloping on the beam, and would not impair the excellent laminarity of the electrostatic beam as shown in Figure 40.

Best results of the magnetic circuit design efforts follow. Figure 41 shows the field due to the super-conducting Helmholtz pair of solenoid coils providing the main focusing field of 35.4 kilogauss. At 4% of the main field there will be a second region of uniform field at 1400 gauss. Figure 39 indicates that this region will indeed be some distance away from the center of the Helmholtz pair. After several iterations on the NUTCRACKER program, the results as shown in Figure 42 indicate that the two regions required in this tube can be constructed without saturating the iron polepieces. In Figure 42 the final coil configuration is also shown.

A solenoid with various polepiece shapes was modeled on the LAPLACE program, with the resulting computed magnetic field then put on the gun simulation program. These results are shown in Figures 43 and 44. The approximate locations at the polepieces are shown in each figure. It was determined that beam scalloping (below 10%) is relatively insensitive to the shape and location of the polepiece. Other measures may have to be investigated if there is a necessity to further decrease the scalloping. In preserving the uniformity in transverse energy of the beam, the magnetic fields simulated caused no more than 0.6% energy spread across the cross-section of the beam. A low transverse energy spread is a prime requirement for high efficiency.

Combination of the two regions of investigation, the gun region and the coil region, cannot be accomplished on either the NUTCRACKER program or the LAPLACE program in a satisfactory manner. However, there exists yet another simulation program known as TRIM, which can handle the combined calculation. There was insufficient time remaining on the current TWT program to warrant initiating a simulation on this computer program.

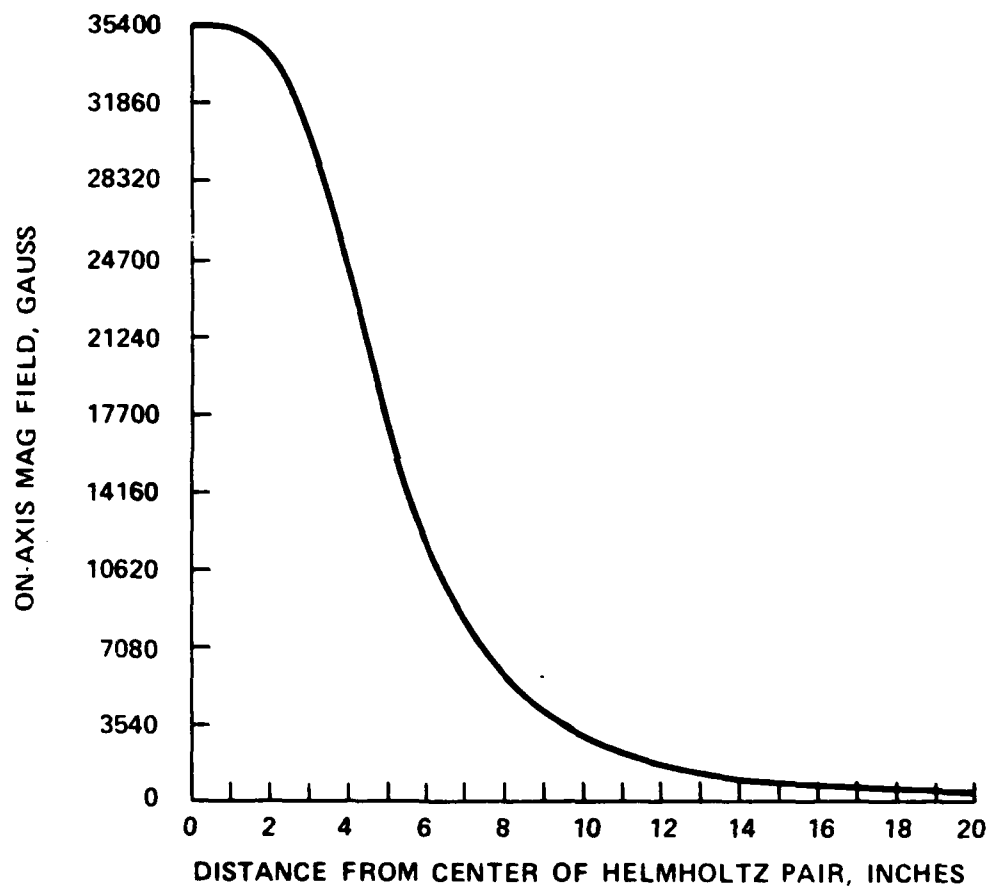


Figure 41. Superconducting Solenoid Field For 94 GHz Tube

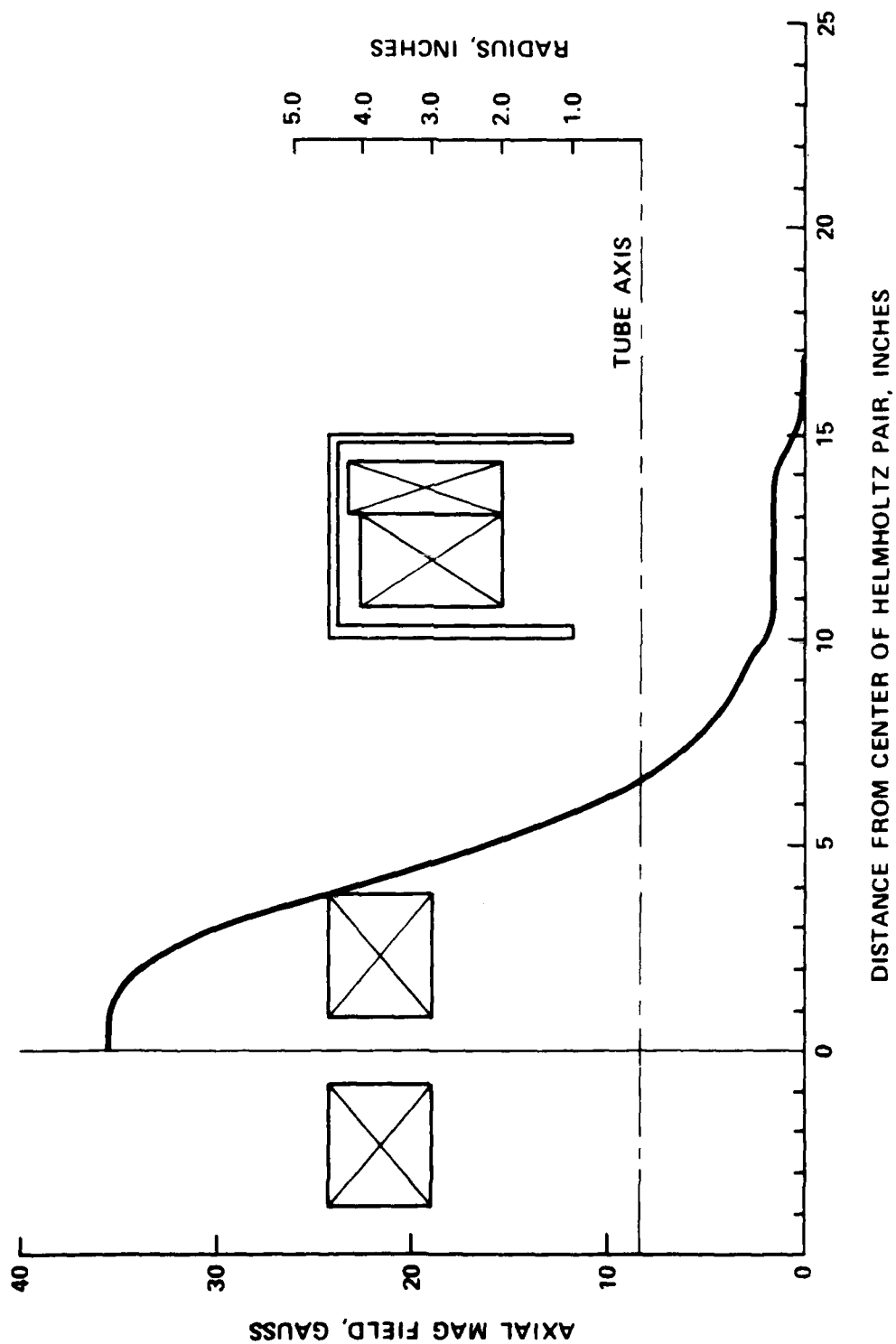


Figure 42. 95 GHz Gyro-TWT Solenoid, Nutcracker Run 4.5

BEAM ANALYSIS:

MICROPERVEANCE = .3370
CURRENT = 4.95A

RADIUS OF 1ST BEAM MINIMUM = $r_b = .10644''$ @ $Z = 0.8''$

% SCALLOP = $\frac{r_{\max} - r_{\min}}{r_{\max} + r_{\min}} \times 100 = 5.3\%$
 $r_{\max} = .119''$
 $r_{\min} = .106''$
 $r_{\text{avg}} = .1125''$

$\frac{V_L}{V} = .56\%$
 $\frac{V_L}{V} \text{ TOTAL}$

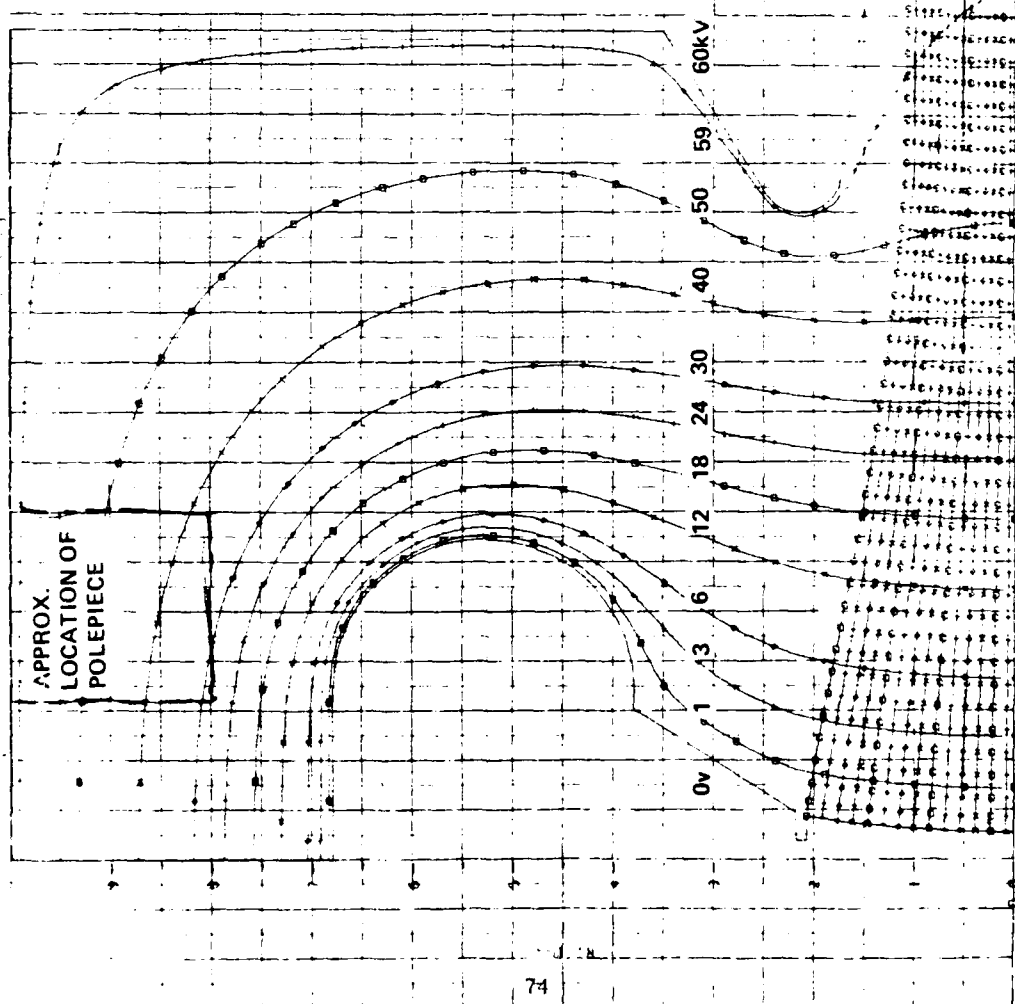
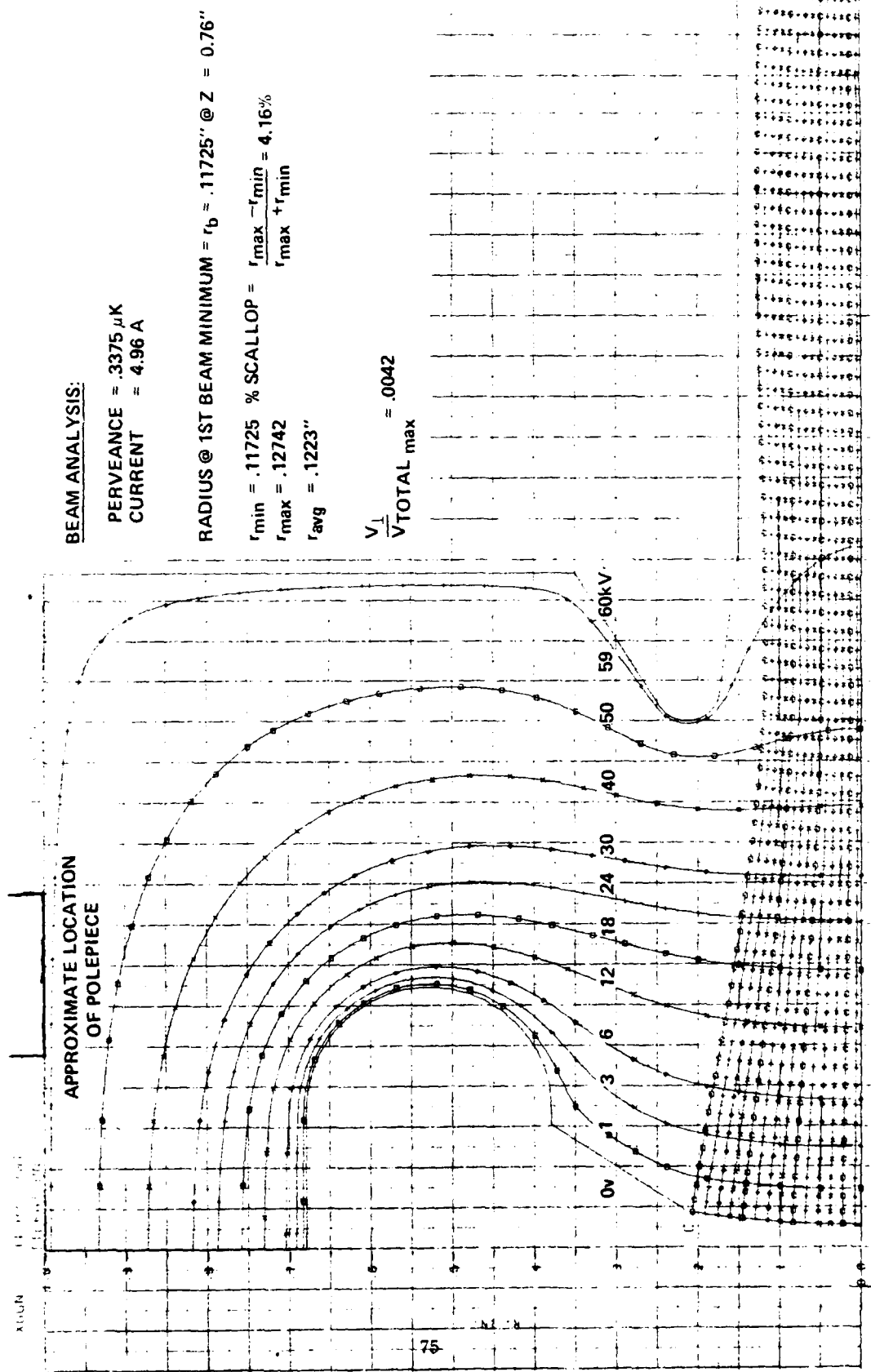


Figure 43. Computed Electron Trajectories For The Pierce-Type Diode Gun For A Magnetic Field With Iron Polepiece ID = 1.67" Located 0.18" From Cathode Center



BEAM ANALYSIS:

PERVEANCE = $.3375 \mu\text{K}$
 CURRENT = 4.96 A

RADIUS @ 1ST BEAM MINIMUM = $r_b = .11725''$ @ $Z = 0.76''$

$r_{\min} = .11725$ % SCALLOP = $\frac{r_{\max} - r_{\min}}{r_{\max} + r_{\min}} = 4.16\%$
 $r_{\max} = .12742$
 $r_{\text{avg}} = .1223''$

$\frac{V_L}{V_{\text{TOTAL max}}} = .0042$

Figure 44. Computed Electron Trajectories For The Pierce-Type Diode Gun For A Magnetic Field With Iron Polepiece ID = $2.09''$, Located $0.27''$ From Cathode Center

7. REFERENCES

1. Millimeter Wave Gyrotron Development, Phase I Final Technical Report. RADC-TR-77-210, June 1977. Contract F30602-76-C-0237, A041596.
2. Zheleznyakov, V. V., "On the Instability of a Magnetoactive Plasma under High-Frequency Electromagnetic Perturbations.I." Izv. VUZ Radiofizika Vol 3, No. 1, p 57 (1960).
3. Gapanov, A. V. and V. K. Yulpatov, "Interaction of Helical Electron Beams with the Electromagnetic Field in a Waveguide," Radiotekhnika i Elektronika, Vol 12, No. 4, p 627 (1967). [Radio Engineering and Electron Physics, Vol 12, No. 4, pp 582-587 (1967)].
4. Ott, E., and M. Manheimer, "Theory of Microwave Emission by Velocity-Space Instabilities of an Intense Relativistic Electron Beam," IEEE Trans. Vol. PS-3 No. 1, pp 1-5 (1975).
5. Sprangle, P and A. T. Drobot, "The Linear and Self-Consistent Non-Linear Theory of the Electron Cyclotron Maser Instability," IEEE Trans. Vol. MTT-25, No. 6, pp 528-544 (1977).
6. Chu, K. R. and A. T. Drobot, "Theory and Single wave Simulation of the Gyrotron Traveling Wave Amplifier Operating at Cyclotron Harmonics," NRL memorandum report 3788 (Aug. 1978).
7. Chu, K. R., A. T. Drobot, H. H. Szu, and P. Sprangle, "Analytic Scaling of Efficiency for the Gyrotron Traveling Wave Amplifier Operating at Cyclotron Harmonics," NRL memorandum report 3892 (May 1979).
8. Development Program for a 200 kW, CW, 28 GHz Gyroklystron, Oak Ridge National Laboratory, Contract No. W-7405 ENG 26.
9. EBT-P 110 GHz Development Program, Oak Ridge National Laboratory, Contract No. W-7405 ENG 26.
10. Kisel, D.V. et al "An Experimental Study of a Gyrotron, Operating at the Second Harmonic of the Cyclotron Frequency, with Optimized Distribution of the High-Frequency Field," Radio Engineering and Electron Physics, Vol. 19 95 (1974).
11. Manuilov, V.M. and Tsmring, S.E., "Synthesis of Axially-Symmetric Systems of the Formation of Helical Electron Beams," Radio Engineering and Electron Physics (Radiotekhnika i Elektronika, p 1486) Vol 23, No. 7. (1978)
12. Septor, J. L., V. L. Granatstein, K. R. Chu, P. Sprangle, and M. E. Read, "The Electron Cyclotron Maser as a High-Power TWT of Millimeter Waves," IEEE Journal of Quantum Electronics, Vol. QE-15, No. 9, pp 848-853 (1979).
13. Wingerson, R. C. "Corkscrew - A Device for Changing the Magnetic Moment of Charged Particles in a Magnetic Field", Phys. Rev. Lett. Vol. 6, 446 (1961).

14. Hirshfield, J. L. and Wachtel, J. M., "Electron Cyclotron Maser," Phys. Rev. Ltrs, Vol. 12, 533 (1964).
15. Bott, I. B., "A Powerful Source of Millimetre Wavelength Electromagnetic Radiation", Phys. Ltrs. Vol. 14, 293 (1965).

APPENDIX

Derivation of perpendicular velocity equation for bifilar helix for arbitrary adiabatic compression.

Consider the schematic diagram of a gyro-TWT using a Pierce-type gun as shown in Figure A-1. Three distinct regions are denoted. From the conservation of energy, at the entrance to the bifilar helix

$$E_{\parallel 0} = E \quad (1)$$

and at the exit of the bifilar helix

$$E_{\parallel 1} + E_{\perp 1} = E \quad (2)$$

In the rf interaction region

$$E_{\parallel 2} + E_{\perp 2} = E \quad (3)$$

where

- E = total energy in the electron beam
- $E_{\parallel i}$ = parallel energy in the i^{th} region
- $E_{\perp i}$ = perpendicular energy in the i^{th} region

Taking the ratio of (2):(3) gives

$$\frac{E_{\parallel 1} + E_{\perp 1}}{E_{\parallel 2} + E_{\perp 2}} = 1 \quad (4)$$

For adiabatic compression the perpendicular energies in Regions 1 and 2 are related by

$$\frac{E_{\perp 1}}{B_1} = \frac{E_{\perp 2}}{B_2} \quad (5)$$

and the electron beam radii are related by

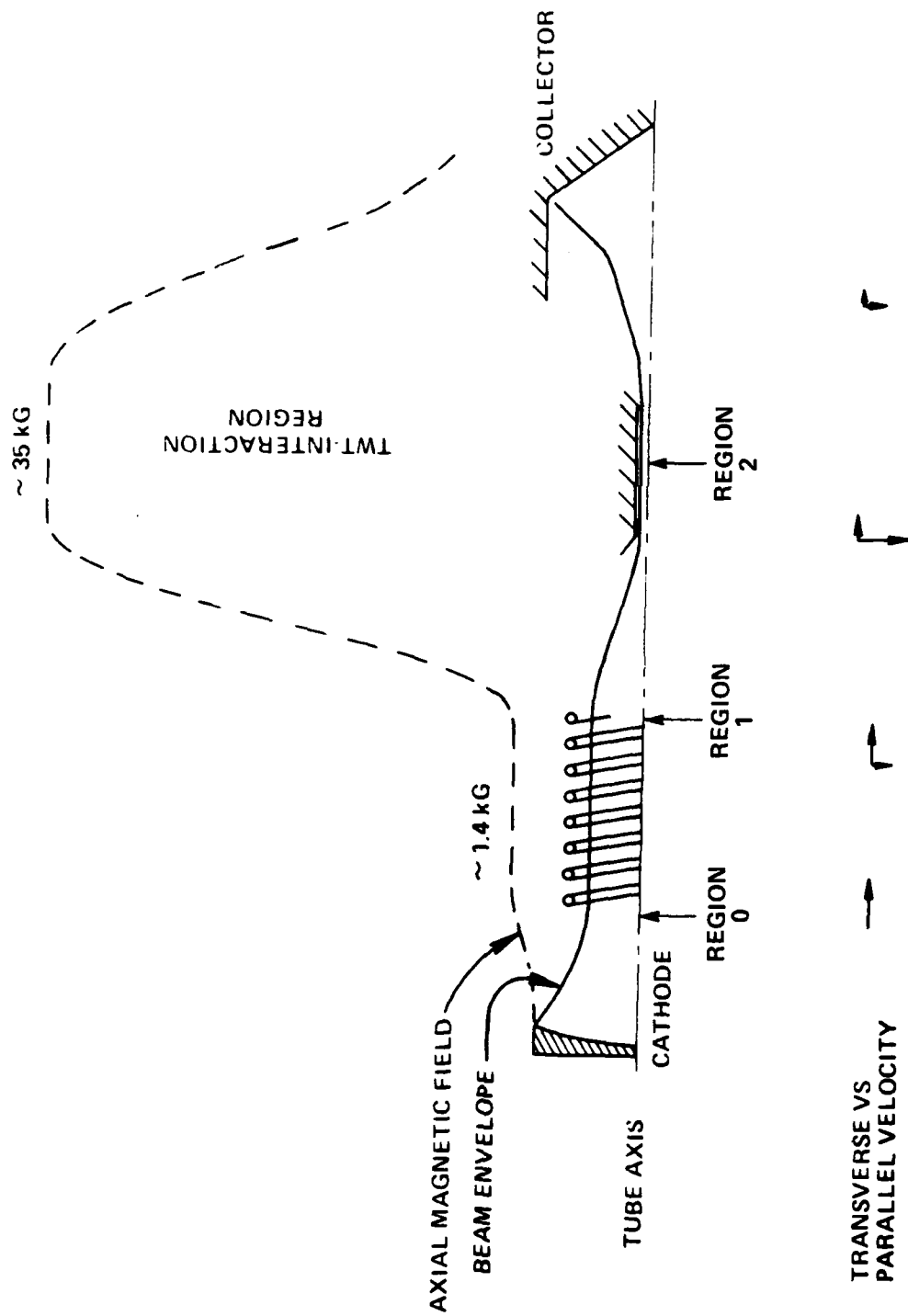


Figure A-1. Schematic Diagram of a Gyro-TWT using a Pierce-Type Electron Gun and Bifilar Helix

$$\left(\frac{R_2}{R_1}\right)^2 = \frac{B_1}{B_2} \quad (7)$$

where B_1 and B_2 are the magnetic fields in regions 1 and 2, respectively. Combining (5) and (6) gives

$$E_{12} = \left(\frac{R_1}{R_2}\right)^2 E_{i1} \quad (8)$$

Substituting (8) into (4) gives

$$\frac{B_{\perp 1}}{B_{\parallel 1}} = \left[\frac{1}{\left(\frac{R_1}{R_2}\right)^2 \left[\left(\frac{v_{\perp 2}}{v_{\parallel 2}}\right)^2 + 1 \right] - 1} \right]^{1/2} \quad (9)$$

where

$$B_{\perp i} = \frac{v_{\perp i}}{c} \quad i = 1, 2$$

$$B_{\parallel i} = \frac{v_{\parallel i}}{c} \quad i = 1, 2$$

The perpendicular and parallel velocities are $v_{\perp i}$ and $v_{\parallel i}$ respectively. Use was made of the relation

$$\left(\frac{\beta_{\perp}}{\beta_{\parallel}}\right)_i^2 = \left(\frac{E_{\perp}}{E_{\parallel}}\right)_i \quad (10)$$

Equation (9) gives the perpendicular velocity to parallel velocity ratio required at the exit of the helix for a given area compression and an assumed velocity ratio in the rf interaction region.



MISSION of Rome Air Development Center

RADC plans and executes research, development, test and selected acquisition programs in support of Command, Control Communications and Intelligence (C³I) activities. Technical and engineering support within areas of technical competence is provided to ESD Program Offices (POs) and other ESD elements. The principal technical mission areas are communications, electromagnetic guidance and control, surveillance of ground and aerospace objects, intelligence data collection and handling, information system technology, ionospheric propagation, solid state sciences, microwave physics and electronic reliability, maintainability and compatibility.